Large in-plane elastic deformations of bi-pantographic fabrics: asymptotic homogenization and experimental validation

Emilio Barchiesi, Simon R Eugster, Francesco Dell'isola, François Hild

Large in-plane elastic deformations of bi-pantographic fabrics: asymptotic homogenisation and experimental validation

Emilio Barchiesi, Simon R. Eugster, Francesco dell'Isola and François Hild

Abstract. Bi-pantographic fabrics are composed of two families of pantographic beams and correspond to a class of architectured materials that are described in plane as second-gradient 2D-continua. On a discrete level, a pantographic beam is a periodic arrangement of cells and looks like an expanding barrier. The materialisation of a bi-pantographic fabrics made by Polyamide was achieved by additive manufacturing techniques. Starting from a discrete spring system, the deformation energy of the corresponding continuum is derived for large strains by asymptotic homogenisation. The obtained energy depends on the second gradient of the deformation through the rate of change in orientation and stretch of material lines directed along the pantographic beams. Displacement-controlled bias extension tests were performed on rectangular prototypes for total elastic extension up to 25%. Force-displacement measurements complemented by local digital image correlation analyses were used to fit the continuum model achieving excellent agreement.

Keywords: variational asymptotic homogenisation, bi-pantographic fabrics, second gradient continua, additive manufacturing, local digital image correlation, Piola's ansatz, experimental mechanics

1. Introduction

Continuum modelling, i.e. spatially continuous formulations [1, 2, 3, 4, 5], is routinely exploited to describe at macro length scales the collective behaviour of – mostly periodic – discrete systems, whose element-by-element micro-scale description [6, 7, 8, 9, 10] can get computationally challenging. Homogenisation procedures [11, 12, 13, 14, 15] can be used to pass from a discrete to a continuous description. These procedures involve the definition of specific micro-macro correspondences [16], which enable to give a precise meaning to many features of the macro-model in terms of those of the micro-model.

The last few decades have witnessed a high acceleration in the development of additive and subtractive techniques such as 3D-printing [17]. Such techniques allow for micro-structure control at very small scales, which motivate the renewed interest in homogenisation [18, 19, 20, 21, 22].

Pantographic structures [23, 24, 25] are among the most straightforward examples of micro-structures whose continuum modelling gives a wealth of non-standard problems in the theory of higher-gradient [26, 27, 28] and micromorphic continua [29, 11, 30, 31], also of mathematical interest [32]. Convenient discrete descriptions of pantographic structures have been obtained in the literature by Hencky-type modelling [30, 7, 8].

The derivation of a 1D-continuum model being capable of describing the finite planar deformation of a discrete slender pantographic structure, referred to as pantographic beam, is presented in [33]. The continuum model is deduced from a discrete one by applying a variational asymptotic procedure [34, 11, 20, 35]. Within the homogenisation process, the overall dimension of the system is kept fixed, while the number of the periodically appearing subsystems – called cells – is increased, and the stiffnesses are appropriately scaled.

In [33], the model of [34, 35] has been generalized to the finite strain regime. Remarkably, the deformation energy density of such a 1D-continuum, [33], does not only depend on the material curvature but also on the stretch gradient. Besides a more pedagogical presentation of such a continuum model, Barchiesi et al. [36] addressed numerically the evaluation of differences between the micro- and the macro-model in order to elucidate to what extent the continuum retains the relevant phenomenology of the discrete system. Special attention has been given to the difference between the deformation energy of the micro- and the macro-model when the micro length scale tends to zero, i.e. the discrete-continuum error. This deviation gives a quantitative value to assess the quality of the approximation of the discrete by its continuous counterpart.

Bi-pantographic fabrics have been first introduced by Seppecher et al. [35] as assemblies of discrete pantographic beams leading at macroscopic scale to second gradient materials [37, 38, 39]. The corresponding deformation energy depends upon the rate of change in orientation and stretch of material lines directed along the pantographic beams. The aims of this work are the following ones. First, we want to generalize the homogenisation carried out in [35] in two respects. In particular, extensible elements and arbitrarily large strains are considered. Secondly, a possible design of bi-pantographic prototypes is sought, which is obeying the discrete model. Lastly, the derived results will be validated.

Addressing the above objectives leads to the following organisation of the paper. In Section 2, the discrete bi-pantographic structure is introduced followed by a homogenisation that is carried out by exploiting the results obtained for pantographic beams. In Section 3, we establish relations between quantities for the microscopic and macroscopic models, which go beyond Piola's micro-macro identification used throughout the homogenisation. Based on these relations, a non-standard bias extension test is then introduced for both models. Lastly, the finite element method employed to solve the continuum model is introduced with a special emphasis on the challenges arising from a weak mixed formulation. In Section 4, the design and manufacturing of a bi-pantographic prototype is reported together with the description of the experimental setup. The Digital Image Correlation (DIC) technique used to retrieve discrete displacement measures is also briefly recalled. In Section 5, the fitting of parameters by means of acquired experimental measures is presented and continuum is compared with experiments.

2. Heuristic homogenisation

The continuum is deduced by applying Piola's micro-macro identification procedure [11, 40], which can be considered as a heuristic variational asymptotic procedure. The steps describing such a procedure can be sketched as:

(i) A family of discrete spring systems embedded in the two-dimensional Euclidean vector space $\mathbb{E}^2$, i.e. the micro-model with micro length scale $\varepsilon > 0$, is introduced – generalized coordinates and energy contributions $\mathfrak{E}_\varepsilon$ are defined

(ii) The kinematic descriptors of the continuum, i.e. the macro-model, are introduced as continuous functions with a closed subset of $\mathbb{E}^2$ as their common domain – these functions must be chosen such that their evaluation at particular points can be related to the generalized coordinates of the micro-model

(iii) Formulation of the deformation energy of the micro-model $\mathfrak{E}_\varepsilon$ using the evaluation of the continuum descriptors at particular points, followed by a Taylor expansion of the energy with respect to the micro length scale ε

(iv) Specification of scaling laws for the constitutive parameters in the micro-model followed by a limit process in which the energy of the continuum $\mathfrak{E}$ is related to the micro-model by $\mathfrak{E} = \lim_{\varepsilon \to 0} \mathfrak{E}_\varepsilon$

2.1. Preliminaries

To ease the presentation, before addressing bi-pantographic structures, some preliminary computations related to pantographic beams are revisited.

Pantographic beam – discrete model. The assembly and kinematics of a discrete pantographic beam slightly generalizing that presented in [33, 36] are sketched in Fig. 1. In the undeformed configuration, see Fig. 1(a), N cells are arranged upon a straight line along the direction of the unit basis vector $e_x \in \mathbb{E}^2$. The total length $L \in \mathbb{R}$ of the undeformed pantographic beam accounts for $N-1$ cells, as depicted in Fig. 1(a). The cells are centred at the positions $P_i = i\varepsilon e_x$ for $i \in \{0, 1, \ldots, N-1\}$ with $\varepsilon = L/(N-1)$. The basic i-th unit cell is formed by four extensional springs hinge-joined together at P_i having length $\varepsilon/(2\cos\gamma)$. Rotational springs, which are coloured in blue, red, and green in Fig. 1(d), are placed between opposite collinear and adjacent springs belonging to the same cell and between adjacent springs belonging to different cells. Note that extensional springs are rigid with respect to bending such that they can transmit torques. White-filled circles in Fig. 1 depict hinge constraints, requiring the end points of the corresponding springs to have the same position in space. We note that the assembly considered herein is a generalization of that studied in [33], as the angle $\gamma \in (0, \pi)$ between springs concurring at point P_i from the right in Fig. [33] is generally different from $\pi/4$. Moreover, further rotational springs, which are coloured in green in Fig. 1(d), are considered. When not otherwise mentioned, the indices i, μ and ν henceforth belong respectively to the following sets: $i \in \{0, 1, \ldots, N-1\}$, $\mu \in \{1, 2\}$ and $\nu \in \{D, S\}$[1].

The kinematics of the spring system is locally described by finitely many generalized coordinates. The coordinates are the positions $p_i \in \mathbb{E}^2$ of the points at position P_i in the reference configuration and the lengths of the oblique deformed springs $l_i^{\mu\nu} \in \mathbb{R}$. Various other kinematical quantities are considered to formulate the total potential
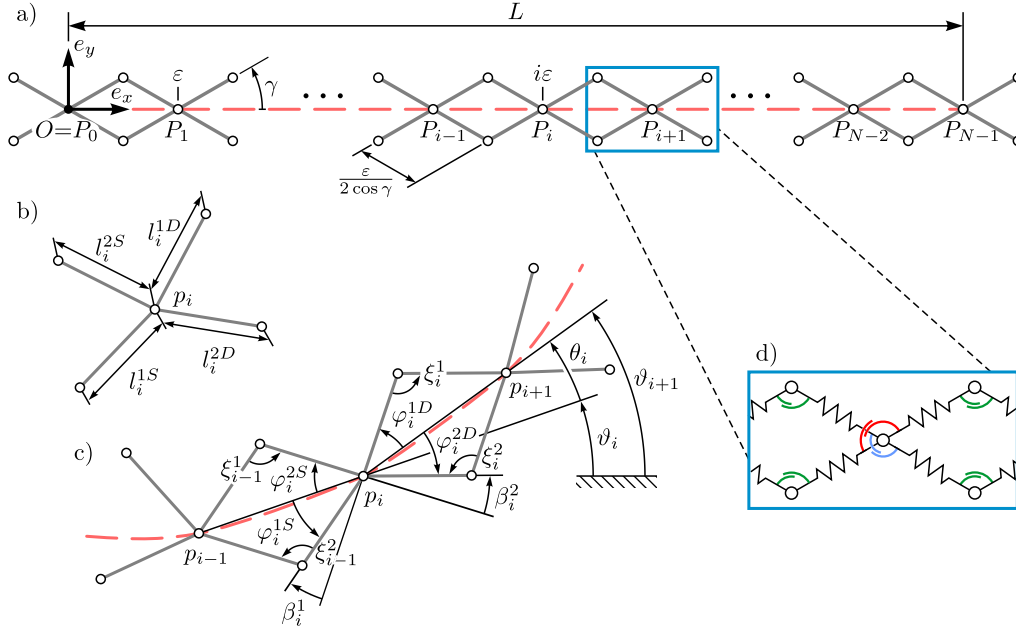
---

[1] D stands for *dextrum*, S for *sinistrum*.

FIGURE 1. Pantographic beam. (a) Undeformed configuration. (b) Generalized coordinates of i-th cell. (c) Deformed configuration with redundant kinematic quantities. (d) Force elements of a single cell.

energy in a most compact form. Applying the law of cosines, the angles $\varphi_i^{\mu\nu}$ depicted in Fig. 1(c) are determined by the following relationships

$$\varphi_i^{1D} = \cos^{-1}\left[\frac{\|p_{i+1}-p_i\|^2 + \left(l_i^{1D}\right)^2 - \left(l_{i+1}^{2S}\right)^2}{2l_i^{1D}\|p_{i+1}-p_i\|}\right] \,,$$

$$\varphi_i^{1S} = \cos^{-1}\left[\frac{\|p_i-p_{i-1}\|^2 + \left(l_i^{1S}\right)^2 - \left(l_{i-1}^{2D}\right)^2}{2l_i^{1S}\|p_i-p_{i-1}\|}\right] \,,$$

$$\varphi_i^{2D} = \cos^{-1}\left[\frac{\|p_{i+1}-p_i\|^2 + \left(l_i^{2D}\right)^2 - \left(l_{i+1}^{1S}\right)^2}{2l_i^{2D}\|p_{i+1}-p_i\|}\right] \,,$$

$$\varphi_i^{2S} = \cos^{-1}\left[\frac{\|p_i-p_{i-1}\|^2 + \left(l_i^{2S}\right)^2 - \left(l_{i-1}^{1D}\right)^2}{2l_i^{2S}\|p_i-p_{i-1}\|}\right] \,,$$

(1)

while the angles ξ_i^μ depicted in Fig. 1(c) are determined by

$$\xi_i^{1(2)} = \cos^{-1}\left[\frac{\left(l_i^{1(2)D}\right)^2 + \left(l_{i+1}^{2(1)S}\right)^2 - \|p_{i+1}-p_i\|^2}{2l_i^{1(2)D}l_{i+1}^{2(1)S}}\right] \,.$$

(2)

For $a \in \mathbb{E}^2$, $\|a\| = \sqrt{a \cdot a}$ corresponds to the norm induced by the inner product denoted by the dot.

Note that $\varphi_0^{\mu S}$ and $\varphi_{N-1}^{\mu D}$ cannot be determined by equations (1) and belong also to the set of generalized coordinates. Another restriction is that the choice of generalized coordinates holds only locally, as long as the angles φ_i^{1D} and φ_i^{2D} do not change sign. Throughout the derivation of the macro-model, it is assumed that the angles φ_i^{1D} and φ_i^{2D} remain in the range $(0,\pi)$. This entails that $\xi_i^\mu \in (0,\pi)$. For the reduced index set $i = \{1, 2, \ldots, N-2\}$, the angle between the two vectors $p_i - p_{i-1}$ and e_x is denoted by ϑ_i. Then the angle θ_i between the vectors $p_i - p_{i-1}$ and $p_{i+1} - p_i$ reads

$$\theta_i = \vartheta_{i+1} - \vartheta_i = \tan^{-1}\left[\frac{(p_{i+1}-p_i)\cdot e_y}{(p_{i+1}-p_i)\cdot e_x}\right] - \tan^{-1}\left[\frac{(p_i-p_{i-1})\cdot e_y}{(p_i-p_{i-1})\cdot e_x}\right] \,.$$

(3)

Let us set $\theta_0 = \theta_1$ and $\theta_{N-1} = \theta_{N-2}$ such that the deviation angles of two adjacent oblique springs from being collinear are given for the entire index set of i by

$$\beta_i^1 = \theta_i + \varphi_i^{1D} - \varphi_i^{1S} \,, \quad \beta_i^2 = \theta_i + \varphi_i^{2S} - \varphi_i^{2D} \,.$$

(4)

For the undeformed configuration, see Fig. 1(a), the following equalities are satisfied

$$l_i^{\mu\nu} = \frac{1}{2\cos\gamma}\varepsilon \,, \quad \beta_i^1 = \beta_i^2 = 0 \,, \quad \|p_i - p_{i-1}\| = \varepsilon \,. \tag{5}$$

Letting the summations for i, μ and ν range over the above introduced sets $\{0, \ldots, N-1\}$, $\{1, 2\}$ and $\{D, S\}$, respectively, the micro-model deformation energy is defined as

$$\mathcal{E}_\varepsilon = \frac{k_E}{2}\sum_i\sum_{\mu,\nu}\left(l_i^{\mu\nu} - \frac{1}{2\cos\gamma}\varepsilon\right)^2 + \frac{k_F}{2}\sum_i\sum_\mu(\beta_i^\mu)^2 + \frac{k_S}{2}\sum_i\sum_\mu(\xi_i^\mu - \pi + 2\gamma)^2$$

$$\stackrel{(4)}{=} \frac{k_E}{2}\sum_i\sum_{\mu,\nu}\left(l_i^{\mu\nu} - \frac{1}{2\cos\gamma}\varepsilon\right)^2 + \frac{k_F}{2}\sum_i\sum_\mu\left[\theta_i + (-1)^\mu\left(\varphi_i^{\mu S} - \varphi_i^{\mu D}\right)\right]^2 + \frac{k_S}{2}\sum_{i=0}^{N-2}\sum_\mu(\xi_i^\mu - \pi + 2\gamma)^2, \tag{6}$$

where $k_E > 0$ and $k_F, k_S > 0$ are the stiffnesses of the extensional and rotational springs, respectively. Boundedness of the deformation energy, both for the micro-model and for the macro-model is considered throughout this paper. It is worth noting that, besides the rigid body modes, the set of admissible configurations defined by

$$l_i^{\mu\nu} = \frac{1}{2\cos\gamma}\varepsilon \,, \quad p_i = p_{i-1} + Ke_x \,, \quad p_0 = P_0 \,, \qquad \text{for } K \in \left(0, \frac{1}{\cos\gamma}\varepsilon\right) \,, \tag{7}$$

also entails null deformation energy when $k_S = 0$, i.e. when removing green springs in Fig. 1(d), and is referred to as extensional floppy mode [34]. Looking at the points p_i, one observes uniform extension or compression.

For the lengths $l_i^{\mu\nu}$ of the oblique springs, the following asymptotic expansion is assumed

$$l_i^{\mu\nu} = \frac{1}{2\cos\gamma}\varepsilon + \varepsilon^2\tilde{l}_i^{\mu\nu} + o(\varepsilon^2) \,, \tag{8}$$

where $\tilde{l}_i^{\mu\nu} \in \mathbb{R}$. Inserting assumption (8) into the energy (6) leads to

$$\mathcal{E}_\varepsilon = \frac{k_E}{2}\sum_i\sum_{\mu,\nu}\left[\varepsilon^2\tilde{l}_i^{\mu\nu} + o(\varepsilon^2)\right]^2 + \frac{k_F}{2}\sum_i\sum_\mu\left[\theta_i + (-1)^\mu\left(\varphi_i^{\mu S} - \varphi_i^{\mu D}\right)\right]^2 + \frac{k_S}{2}\sum_i\sum_\mu(\xi_i^\mu - \pi + 2\gamma)^2. \tag{9}$$

Pantographic beam – micro-macro identification. The slenderness of the discrete system makes it reasonable to aim for a one-dimensional continuum [41] in the limit of vanishing ε. The continuum is then parametrised by the arclength $s \in [0, L]$ of the straight segment of length L connecting all points P_i.

The independent kinematic Lagrangian descriptors of the macro-model are assumed to be the functions $\chi : [0, L] \to \mathbb{E}^2$ and $\tilde{l}^{\mu\nu} : [0, L] \to \mathbb{R}$. The placement function χ places the 1D-continuum into $\mathbb{E}^2$ and is best suited to describe the points $p_i \in \mathbb{E}^2$ of the discrete system on a macro-level. To take into account also the effect of changing spring lengths $\tilde{l}_i^{\mu\nu}$ introduced in equation (8), the placement function is augmented by the four micro-strain functions $\tilde{l}^{\mu\nu}$. The identification of the discrete system is possible with a one-dimensional continuum that is classified as a micromorphic continuum [42, 43, 44, 45]. It is also convenient to introduce the functions $\rho : [0, L] \to \mathbb{R}^+$ and $\vartheta : [0, L] \to [0, 2\pi)$ in order to rewrite the tangent vector field χ' to the deformed 1D-continuum as

$$\chi'(s) = \rho(s)\left[\cos\vartheta(s)e_x + \sin\vartheta(s)e_y\right] \,, \tag{10}$$

where prime denotes differentiation with respect to the reference arc length s. Thus ρ corresponds to the norm of the tangent vector $\|\chi'\|$ and is referred to as stretch. The current curve $\chi([0, L])$ can, in general, have a length $\int_0^L \rho \, ds$ different from L, as s is not an arc-length parametrisation for χ but for the reference placement $\chi_0(s) = se_x$. Introducing the normal vector field $\chi'_\perp(s) = \rho(s)\left[-\sin\vartheta(s)e_x + \cos\vartheta(s)e_y\right]$, being rotated against $\chi'(s)$ about 90° in the anti-clockwise direction, the following results are found

$$\rho'(s) = \frac{\chi'(s) \cdot \chi''(s)}{\|\chi'(s)\|} \,, \qquad \vartheta'(s) = \frac{\chi''(s) \cdot \chi'_\perp(s)}{\|\chi'(s)\|^2} \,. \tag{11}$$

In the sequel ρ' and ϑ' are called stretch gradient and material curvature, respectively. For Piola's micro-macro identification the generalized coordinates of the discrete system are related to the functions χ and $\tilde{l}^{\mu\nu}$ evaluated at $s_i = i\varepsilon$ as

$$\chi(s_i) = p_i \,, \qquad \tilde{l}^{\mu\nu}(s_i) = \tilde{l}_i^{\mu\nu} \,. \tag{12}$$

For the asymptotic identification, the energy (9) is expanded in ε. The expansion of χ is given by

$$\chi(s_{i\pm1}) = \chi(s_i) \pm \varepsilon\chi'(s_i) + \frac{\varepsilon^2}{2}\chi''(s_i) + o(\varepsilon^2) \,. \tag{13}$$

Combining the asymptotic expansion (8) with $(12)_2$ and the expansion $\tilde{l}^{\mu\nu}(s_{i\pm1}) = \tilde{l}^{\mu\nu}(s_i) + o(\varepsilon^0)$, leads to

$$l_{i\pm1}^{\mu\nu} = \frac{1}{2\cos\gamma}\varepsilon + \tilde{l}^{\mu\nu}(s_i)\varepsilon^2 + o(\varepsilon^2) \ . \tag{14}$$

In order to further expand (9), the terms θ_i, $\varphi_i^{\mu S} - \varphi_i^{\mu D}$ and ξ_i^μ are expanded up to first order (see App. A). For θ_i according to equation (71)

$$\theta_i = \vartheta'(s_i)\varepsilon + o(\varepsilon) \ . \tag{15}$$

The differences $\varphi_i^{1(2)S} - \varphi_i^{1(2)D}$ are given by equation (78) as

$$\varphi_i^{1(2)S} - \varphi_i^{1(2)D} = \left. \frac{4[\rho^2 - (1/2\cos^2\gamma)](\tilde{l}^{1(2)S} - \tilde{l}^{1(2)D}) + (1/\cos\gamma)(\rho^2)' + (2/\cos^2\gamma)(\tilde{l}^{2(1)D} - \tilde{l}^{2(1)S})}{4\rho(1/2\cos\gamma)\sqrt{(1/\cos^2\gamma) - \rho^2}} \right|_{s=s_i} \varepsilon + o(\varepsilon) \ . \tag{16}$$

The angles ξ_i^μ are given by (80) as

$$\xi_i^\mu = \left. \cos^{-1}\left(1 - \frac{\rho^2}{1/2\cos^2\gamma}\right)\right|_{s=s_i} + o(\varepsilon^0) \ . \tag{17}$$

Substituting (15), (16) and (17) into (9) together with $\rho(s_i) = \|\chi'(s_i)\|$, the sought expansion of the micro-model energy $\mathcal{E}_\varepsilon$ as a function of the kinematic descriptors χ and $\tilde{l}^{\mu\nu}$ reads

$$\begin{aligned}
\mathcal{E}_\varepsilon &= \sum_i \left\{ \frac{k_E\varepsilon^4}{2}\left[\sum_{\mu,\nu}\left(\tilde{l}^{\mu\nu}\right)^2 + o(\varepsilon^0)\right] + k_S\left[\cos^{-1}\left(1 - \frac{\rho^2}{1/2\cos^2\gamma}\right) - \pi + 2\gamma + o(\varepsilon^0)\right]^2 \right\}_{s=s_i} \\
&+ \sum_i \frac{k_F\varepsilon^2}{2}\left[\vartheta' + \frac{4[\rho^2 - (1/2\cos^2\gamma)](\tilde{l}^{1S} - \tilde{l}^{1D}) + (1/\cos\gamma)(\rho^2)' + (2/\cos^2\gamma)(\tilde{l}^{2D} - \tilde{l}^{2S})}{4\rho(1/2\cos\gamma)\sqrt{(1/\cos^2\gamma) - \rho^2}} + o(\varepsilon^0)\right]_{s=s_i}^2 \\
&+ \sum_i \frac{k_F\varepsilon^2}{2}\left[\vartheta' + \frac{4[\rho^2 - (1/2\cos^2\gamma)](\tilde{l}^{2S} - \tilde{l}^{2D}) + (1/\cos\gamma)(\rho^2)' + (2/\cos^2\gamma)(\tilde{l}^{1D} - \tilde{l}^{1S})}{4\rho(1/2\cos\gamma)\sqrt{(1/\cos^2\gamma) - \rho^2}} + o(\varepsilon^0)\right]_{s=s_i}^2 \ .
\end{aligned} \tag{18}$$

Let the parameters $K_E, K_F, K_S > 0$ be constants, which do not depend on ε. Then they are related to the stiffnesses of each discrete system with micro length scale ε by a scaling law

$$k_E = K_E\varepsilon^{-3} \ , \qquad k_F = K_F\varepsilon^{-1} \ , \qquad k_S = K_S\varepsilon \ . \tag{19}$$

Pantographic beam – macro-model. The continuum limit is now obtained by letting $\varepsilon \to 0$. The deformation energy for the homogenised macro-model becomes

$$\begin{aligned}
\mathcal{E} &= \int_0^L \left\{ K_S\left[\cos^{-1}\left(1 - \frac{\rho^2}{1/2\cos^2\gamma}\right) - \pi + 2\gamma\right]^2 + \frac{K_E}{2}\sum_{\mu\nu}\left(\tilde{l}^{\mu\nu}\right)^2 \right\}\mathrm{d}s \\
&+ \int_0^L \frac{K_F}{2}\left[\vartheta' + \frac{4[\rho^2 - (1/2\cos^2\gamma)](\tilde{l}^{1S} - \tilde{l}^{1D}) + (1/\cos\gamma)(\rho^2)' + (2/\cos^2\gamma)(\tilde{l}^{2D} - \tilde{l}^{2S})}{4\rho(1/2\cos\gamma)\sqrt{(1/\cos^2\gamma) - \rho^2}}\right]^2\mathrm{d}s \\
&+ \int_0^L \frac{K_F}{2}\left[\vartheta' + \frac{4[\rho^2 - (1/2\cos^2\gamma)](\tilde{l}^{2S} - \tilde{l}^{2D}) + (1/\cos\gamma)(\rho^2)' + (2/\cos^2\gamma)(\tilde{l}^{1D} - \tilde{l}^{1S})}{4\rho(1/2\cos\gamma)\sqrt{(1/\cos^2\gamma) - \rho^2}}\right]^2\mathrm{d}s \ .
\end{aligned} \tag{20}$$

The basic properties of the energy are preserved during the asymptotic process. Both the energy of the micro- and the macro-model (6) and (20), respectively, are invariant under superimposed rigid body motions. Also the extensional floppy mode of the discrete model, see (7), transfers to the continuum. Namely, if $\rho' = \vartheta' = \tilde{l}^{\mu\nu} = 0$ and $\rho(s) = 1$, then the deformation energy vanishes. When $K_S = 0$, if $\rho' = \vartheta' = \tilde{l}^{\mu\nu} = 0$, a constant stretch $\rho(s) = K \in (0, 1/\cos\gamma)$ can still be present without causing the deformation energy being different from zero.

Let us now define the deformation energy density Ψ as the integrand of (20). For the energy to be stationary, the necessary conditions are obtained by equating to zero the variation of the deformation energy functional (20) with respect to admissible variations in the independent kinematic descriptors. At this stage, only the variation with respect to $\tilde{l}^{\mu\nu}$ is carried out. This results in a linear system of four algebraic equations given by $\partial\Psi/\partial\tilde{l}^{\mu\nu} = 0$ in which $\tilde{l}^{\mu\nu}$ are the unknowns. Introducing the abbreviations

$$C_1 = \frac{K_F}{2K_F\rho^2 - 1/4\cos^2\gamma\,(K_E\rho^2 + 8K_F)} \ , \qquad C_2 = \frac{K_F\sqrt{1/\cos^2\gamma - \rho^2}}{K_E(1/4\cos^2\gamma)\rho^2 - 2K_F\rho^2 - 4K_E(1/16\cos^4\gamma)} \ , \tag{21}$$

necessary conditions for equilibrium are that

$$\tilde{l}^{\mu D} = \frac{1}{2\cos\gamma}\rho\left[\rho' C_1 + (-1)^{\mu-1}\vartheta' C_2\right], \qquad \tilde{l}^{\mu S} = \frac{1}{2\cos\gamma}\rho\left[-\rho' C_1 + (-1)^{\mu}\vartheta' C_2\right] \ . \tag{22}$$

By substituting the results (22) into (20), a kinematic reduction is performed resulting in the deformation energy functional of the pantographic beam

$$\mathcal{E} = \int_0^L \left\{ K_E K_F \left[\frac{\rho^2 \cos^2\gamma - 1}{\rho^2 \cos^2\gamma \left(K_E - 8K_F \cos^2\gamma\right) - K_E} \vartheta'^2 \right.\right.$$
$$\left.\left. + \frac{\rho^2 \cos^2\gamma}{(1 - \rho^2 \cos^2\gamma)\left[8K_F + \rho^2\left(K_E - 8K_F\cos^2\gamma\right)\right]}\rho'^2 \right] + K_S \left[\cos^{-1}\left(1 - \frac{\rho^2}{1/2\cos^2\gamma}\right) - \pi + 2\gamma\right]^2 \right\}\mathrm{d}s \ , \tag{23}$$

which merely depends on the placement function χ. The energy (23) is positive definite for $0 < \rho < 1/\cos\gamma$ and the complete second gradient χ'' of χ contributes to the deformation energy. Besides the term $\left(\chi'_\perp \cdot \chi''\right)$ being related to the material curvature ϑ' by means of $(11)_1$, also the term $\left(\chi' \cdot \chi''\right)$ appears, which in turn is related to the stretch gradient ρ' given by $(23)_2$. It is also worth noting that, if $\rho(x) = 1/\cos\gamma$, then the term multiplying ϑ' in (23) vanishes. Consequently, at point $s = s_0$ the beam undergoes a beam-to-cable transition, being curvature no more energetically penalized. At the same time, if $\rho(s_0) = 1/\cos\gamma$ then the term multiplying ρ' in (23) diverges. Therefore, boundedness of energy requires $\rho'(s_0) = 0$.

2.2. Bi-pantographic fabrics – discrete model

The assembly of a discrete bi-pantographic fabric is sketched in Fig. 2(b). The kinematics (and employed notation thereof) of discrete bi-pantographic fabrics is given by generalizing that of pantographic beams once the bi-pantographic structure is regarded as an assembly of two identical orthogonal families of parallel equi-spaced pantographic beams hinge joined at their intersection points. Thus, aimed at avoiding unwieldy pictures, we omit to show it in Fig. 2.

In the undeformed configuration, see Fig. 2(a), cells are arranged within the reference domain Ω upon straight lines in direction of the unit basis vectors $e_x, e_y \in \mathbb{E}^2$. The set $\Omega \subseteq \mathbb{R}^2$ is in general a non-simple reference domain with boundary $\partial\Omega$ being the disjoint union of $N_\Omega \in \mathbb{N}$ smooth line sets $\partial\Omega_k$, $k \in [1; N_\Omega]$, pairwise intersecting in distinct vertices belonging to the set $[\partial\partial\Omega]$. A discussion on smoothness requirements for Ω is beyond the scope of this paper. For such a discussion the reader is referred to [46]. The cells are centred at the positions $P_{i,j} = i\varepsilon e_x + j\varepsilon e_y$ – see Fig. 2(b). The basic (i,j)-th unit cell – see Fig. 2(c) – is formed by eight extensional springs hinge-joined together at $P_{i,j}$ having length $\varepsilon/(2\cos\gamma)$. Rotational springs – which are coloured in blue, red, and green in Fig. 2(c) – are placed between opposite collinear adjacent springs belonging to the same cell and between adjacent springs belonging to different cells. The kinematics of the spring system is locally described by finitely many generalized coordinates. The coordinates are the positions $p_{i,j} \in \mathbb{E}^2$ of the points at position $P_{i,j}$ in the reference configuration (equivalently one can consider the nodal displacements $u_{i,j} \in \mathbb{R}^2$ such that $u_{i,j} = p_{i,j} - P_{i,j}$) and the lengths of the oblique deformed springs $l^{\mu\nu}_{(i,j),\alpha} \in \mathbb{R}$, $\alpha \in x,y$. The index α will be henceforth employed to distinguish quantities related to pantographic beams directed along e_x ($\alpha = x$) and e_y ($\alpha = y$). Various other kinematical quantities are introduced to formulate the total potential energy in a most compact form. Applying the law of cosines, the angles $\varphi^{\mu\nu}_{(i,j),\alpha}$ are determined by

$$\varphi^{1D}_{(i,j),x} = \cos^{-1}\left[\frac{\|p_{i+1,j} - p_{i,j}\|^2 + \left(l^{1D}_{(i,j),x}\right)^2 - \left(l^{2S}_{(i+1,j),x}\right)^2}{2l^{1D}_{(i,j),x}\|p_{i+1,j} - p_{i,j}\|}\right] \ ,$$

$$\varphi^{1S}_{(i,j),x} = \cos^{-1}\left[\frac{\|p_{i,j} - p_{i-1,j}\|^2 + \left(l^{1S}_{(i,j),x}\right)^2 - \left(l^{2D}_{(i-1,j),x}\right)^2}{2l^{1S}_{(i,j),x}\|p_{i,j} - p_{i-1,j}\|}\right] \ ,$$

$$\varphi^{2D}_{(i,j),x} = \cos^{-1}\left[\frac{\|p_{i+1,j} - p_{i,j}\|^2 + \left(l^{2D}_{(i,j),x}\right)^2 - \left(l^{1S}_{(i+1,j),x}\right)^2}{2l^{2D}_{(i,j),x}\|p_{i+1,j} - p_{i,j}\|}\right] \ , \tag{24}$$

$$\varphi^{2S}_{(i,j),x} = \cos^{-1}\left[\frac{\|p_{i,j} - p_{i-1,j}\|^2 + \left(l^{2S}_{(i,j),x}\right)^2 - \left(l^{1D}_{(i-1,j),x}\right)^2}{2l^{2S}_{(i,j),x}\|p_{i,j} - p_{i-1,j}\|}\right] \ ,$$
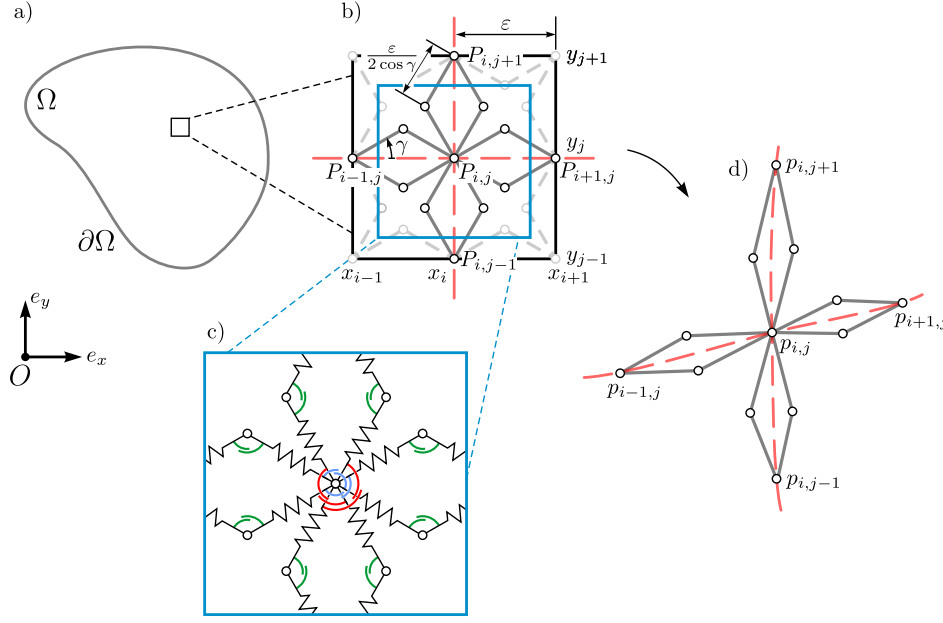
FIGURE 2. Bi-pantographic fabrics. (a) Domain Ω. (b) Undeformed configuration of (i,j)-th cell (including neighbouring elements). (c) Force elements of a single cell. (d) Deformed configuration of (i,j)-th cell (including neighbouring elements).

and

$$
\varphi_{(i,j),y}^{1D} = \cos^{-1} \left[\frac{\|p_{i,j+1} - p_{i,j}\|^2 + \left(l_{(i,j),y}^{1D}\right)^2 - \left(l_{(i,j+1),y}^{2S}\right)^2}{2l_{(i,j),y}^{1D}\|p_{i,j+1} - p_{i,j}\|} \right],
$$

$$
\varphi_{(i,j),y}^{1S} = \cos^{-1} \left[\frac{\|p_{i,j} - p_{i,j-1}\|^2 + \left(l_{(i,j),y}^{1S}\right)^2 - \left(l_{(i,j-1),y}^{2D}\right)^2}{2l_{(i,j),y}^{1S}\|p_{i,j} - p_{i,j-1}\|} \right],
$$

$$
\varphi_{(i,j),y}^{2D} = \cos^{-1} \left[\frac{\|p_{i,j+1} - p_{i,j}\|^2 + \left(l_{(i,j),y}^{2D}\right)^2 - \left(l_{(i,j+1),y}^{1S}\right)^2}{2l_{(i,j),y}^{2D}\|p_{i,j+1} - p_{i,j}\|} \right], \tag{25}
$$

$$
\varphi_{(i,j),y}^{2S} = \cos^{-1} \left[\frac{\|p_{i,j} - p_{i,j-1}\|^2 + \left(l_{(i,j),y}^{2S}\right)^2 - \left(l_{(i,j-1),x}^{1D}\right)^2}{2l_{(i,j),y}^{2S}\|p_{i,j} - p_{i,j-1}\|} \right],
$$

while the angles $\xi_{(i,j),\alpha}^{\mu}$ become

$$
\xi_{(i,j),x}^{1(2)} = \cos^{-1} \left[\frac{\left(l_{(i,j),x}^{1(2)D}\right)^2 + \left(l_{(i+1,j),x}^{2(1)S}\right)^2 - \|p_{i+1,j} - p_{i,j}\|^2}{2l_{(i,j),x}^{1(2)D} l_{(i+1,j),x}^{2(1)S}} \right],
$$

$$
\xi_{(i,j),y}^{1(2)} = \cos^{-1} \left[\frac{\left(l_{(i,j),y}^{1(2)D}\right)^2 + \left(l_{(i,j+1),y}^{2(1)S}\right)^2 - \|p_{i,j+1} - p_{i,j}\|^2}{2l_{(i,j),y}^{1(2)D} l_{(i,j+1),y}^{2(1)S}} \right]. \tag{26}
$$

Having used the law of cosines to determine $\varphi_{(i,j),\alpha}^{\mu\nu}$, the choice of generalized coordinates holds only locally as long as the angles $\varphi_{(i,j),\alpha}^{1D}$ and $\varphi_{(i,j),\alpha}^{2D}$ do not change sign. Throughout the derivation of the macro-model, it is assumed that the angles $\varphi_{(i,j),\alpha}^{1D}$ and $\varphi_{(i,j),\alpha}^{2D}$ remain in the range $(0, \pi)$. This entails that $\xi_{(i,j),\alpha}^{\mu} \in (0, \pi)$. The angle between the two vectors $p_{i,j} - p_{i-1,j}$ and e_x is denoted by $\vartheta_{(i,j),x}$, while the angle between the two vectors $p_{i,j} - p_{i,j-1}$ and e_y is denoted by $\vartheta_{(i,j),y}$. Then the angle $\theta_{(i,j),x}$ between the vectors $p_{i,j} - p_{i-1,j}$ and $p_{i+1,j} - p_{i,j}$ becomes

$$
\theta_{(i,j),x} = \vartheta_{(i+1,j),x} - \vartheta_{(i,j),x} = \tan^{-1} \left[\frac{(p_{i+1,j} - p_{i,j}) \cdot e_y}{(p_{i+1,j} - p_{i,j}) \cdot e_x} \right] - \tan^{-1} \left[\frac{(p_{i,j} - p_{i-1,j}) \cdot e_y}{(p_{i,j} - p_{i-1,j}) \cdot e_x} \right], \tag{27}
$$

while the angle $\theta_{(i,j),y}$ between the vectors $p_{i,j} - p_{i,j-1}$ and $p_{i,j+1} - p_{i,j}$ reads

$$\theta_{(i,j),y} = \vartheta_{(i,j+1),y} - \vartheta_{(i,j),y} = \tan^{-1}\left[\frac{(p_{i,j+1} - p_{i,j}) \cdot e_y}{(p_{i,j+1} - p_{i,j}) \cdot e_x}\right] - \tan^{-1}\left[\frac{(p_{i,j} - p_{i,j-1}) \cdot e_y}{(p_{i,j} - p_{i,j-1}) \cdot e_x}\right]. \tag{28}$$

The following relations hold true

$$\beta^1_{(i,j),\alpha} = \theta_{(i,j),\alpha} + \varphi^{1D}_{(i,j),\alpha} - \varphi^{1S}_{(i,j),\alpha}\,, \quad \beta^2_{(i,j),\alpha} = \theta_{(i,j),\alpha} + \varphi^{2S}_{(i,j),\alpha} - \varphi^{2D}_{(i,j),\alpha}\,. \tag{29}$$

Letting the summations for μ, ν and α range over the sets $\{1,2\}$, $\{D,S\}$ and $\{x,y\}$, respectively, and those for (i,j) over a set such that all energy contributions due to elastic elements in Ω are included in the subsequent formula, the micro-model deformation energy is defined as

$$\begin{aligned}
\mathfrak{E}_\varepsilon &= \frac{k_E}{2}\sum_{i,j}\sum_\alpha\left[\sum_{\mu,\nu}\left(l^{\mu\nu}_{(i,j),\alpha} - \frac{1}{2\cos\gamma}\varepsilon\right)^2 + \frac{k_F}{2}\sum_\mu\left(\beta^\mu_{(i,j),\alpha}\right)^2 + \frac{k_S}{2}\sum_\mu(\xi^\mu_{(i,j),\alpha} - \pi + 2\gamma)^2\right] \\
&\stackrel{(29)}{=} \frac{k_E}{2}\sum_{i,j}\sum_\alpha\Bigg\{\sum_{\mu,\nu}\left(l^{\mu\nu}_{(i,j),\alpha} - \frac{1}{2\cos\gamma}\varepsilon\right)^2 \\
&\quad + \frac{k_F}{2}\sum_\mu\left[\theta_{(i,j),\alpha} + (-1)^\mu\left(\varphi^{\mu S}_{(i,j),\alpha} - \varphi^{\mu D}_{(i,j),\alpha}\right)\right]^2 + \frac{k_S}{2}\sum_\mu(\xi^\mu_{(i,j),\alpha} - \pi + 2\gamma)^2\Bigg\},
\end{aligned} \tag{30}$$

with $k_E > 0$ and $k_F, k_S > 0$ being the stiffnesses of the extensional and rotational springs, respectively. The summand in (6) for the sum over (i,j) will be henceforth denoted by $\Psi_{i,j}$.

It is worth noting that, when $k_S = 0$, besides the rigid body modes also the set of admissible configurations obtained as all possible combinations of 1) uniform shear, i.e. the angle between the centrelines of the two families of pantographic beams is uniform and ranging from $0°$ to $180°$ (pantographic beams are transformed rigidly, and hence this gives an infinite family of floppy modes parametrised on a single parameter that is the above mentioned angle; when a bias rectangular specimen is considered − i.e. fibers form $\pm 45°$ with the sides − this deformation mode corresponds to uniform extension/compression of the rectangle) and 2) extensional floppy mode of constituting pantographic beams entails null deformation energy. For more details on floppy modes in bi-pantographic structures the reader is referred to [35]. While each pantographic beam − as well as pantographic fabrics (whose only non-rigid zero energy deformation mode is given by uniform macroscopic shear; pantographic beams are replaced by (extensible) Elasticae that cannot extend with zero energy) − admits an infinite family of extensional floppy modes parametrised over a single parameter (see equation (7)), the bi-pantographic structure admits an infinite family of floppy modes parametrised over four parameters, see Fig. 11 in [35].

For the lengths $l^{\mu\nu}_{(i,j),\alpha}$ of the oblique springs, the following asymptotic expansion is assumed

$$l^{\mu\nu}_{(i,j),\alpha} = \frac{1}{2\cos\gamma}\varepsilon + \varepsilon^2 \tilde{l}^{\mu\nu}_{(i,j),\alpha} + o(\varepsilon^2)\,, \tag{31}$$

where $\tilde{l}^{\mu\nu}_{(i,j),\alpha} \in \mathbb{R}$. Inserting assumption (31) into the energy (30) leads to

$$\mathfrak{E}_\varepsilon = \sum_\alpha\sum_{i,j}\Bigg\{\frac{k_E}{2}\sum_{\mu,\nu}\left[\varepsilon^2\tilde{l}^{\mu\nu}_{(i,j),\alpha} + o(\varepsilon^2)\right]^2 + \frac{k_F}{2}\sum_\mu\left[\theta_{(i,j),\alpha} + (-1)^\mu\left(\varphi^{\mu S}_{(i,j),\alpha} - \varphi^{\mu D}_{(i,j),\alpha}\right)\right]^2 + \frac{k_S}{2}\sum_\mu(\xi^\mu_{(i,j),\alpha} - \pi + 2\gamma)^2\Bigg\}. \tag{32}$$

2.3. Bi-pantographic fabrics − micro-macro identification

The two-dimensional extension of the discrete system makes it reasonable to aim for a two-dimensional continuum in the limit of vanishing ε. The independent kinematic Lagrangian descriptors of the macro-model are assumed to be the functions $\chi : \Omega \to \mathbb{E}^2$ and $\tilde{l}^{\mu\nu}_\alpha : \Omega \to \mathbb{R}$. The placement function χ places the 2D-continuum into $\mathbb{E}^2$ and is best suited to describe the points $p_{i,j} \in \mathbb{E}^2$ of the discrete system on the macro-level. To take into account the effect of changing spring lengths $\tilde{l}^{\mu\nu}_{(i,j),\alpha}$ introduced in (8), the placement function is augmented by the eight micro-strain functions $\tilde{l}^{\mu\nu}_\alpha$. The identification of the discrete system with a two-dimensional continuum is also classified as a micromorphic continuum [42, 43, 44, 45].

It is also convenient to introduce the functions $\rho_\alpha : \Omega \to \mathbb{R}^+$ and $\vartheta_\alpha : \Omega \to [0, 2\pi)$ in order to rewrite the tangent vector field $\partial\chi/\partial\alpha$ to deformed material lines oriented along e_α in the reference configuration as

$$\frac{\partial\chi}{\partial x}(x,y) = \rho_x(x,y)\left\{[\cos\vartheta_x(x,y)]\,e_x + [\sin\vartheta_x(x,y)]\,e_y\right\}\ ,$$
$$\frac{\partial\chi}{\partial y}(x,y) = \rho_y(x,y)\left\{[\cos\vartheta_y(x,y)]\,e_y + [\sin\vartheta_y(x,y)]\,e_x\right\}\ . \tag{33}$$

Thus ρ_α corresponds to the norm of the tangent vector $\|\partial\chi/\partial\alpha\|$ to the deformed material lines directed along e_α in the reference configuration, and it is referred to as α-stretch. Introducing the normal vector fields to deformed material lines directed, respectively, along e_x and e_y in the reference configuration

$$\left(\frac{\partial\chi}{\partial x}\right)_\perp(x,y) = \rho_x(x,y)\left\{-[\sin\vartheta_x(x,y)]\,e_x + [\cos\vartheta_x(x,y)]\,e_y\right\}\ ,$$
$$\left(\frac{\partial\chi}{\partial y}\right)_\perp(x,y) = \rho_y(x,y)\left\{-[\sin\vartheta_y(x,y)]\,e_y + [\cos\vartheta_y(x,y)]\,e_x\right\}\ , \tag{34}$$

being respectively rotated against $\partial\chi/\partial x$ and $\partial\chi/\partial y$ about 90° in the anti-clockwise direction, it is found that

$$\frac{\partial\rho_x}{\partial x}(x,y) = \frac{\frac{\partial\chi}{\partial x}(x,y)\cdot\frac{\partial^2\chi}{\partial x^2}(x,y)}{\|\frac{\partial\chi}{\partial x}(x,y)\|}\ ,\qquad \frac{\partial\vartheta_x}{\partial x}(x,y) = \frac{\frac{\partial^2\chi}{\partial x^2}(x,y)\cdot\left(\frac{\partial\chi}{\partial x}\right)_\perp(x,y)}{\|\frac{\partial\chi}{\partial x}(x,y)\|^2}\ ,$$
$$\frac{\partial\rho_y}{\partial y}(x,y) = \frac{\frac{\partial\chi}{\partial y}(x,y)\cdot\frac{\partial^2\chi}{\partial y^2}(x,y)}{\|\frac{\partial\chi}{\partial y}(x,y)\|}\ ,\qquad \frac{\partial\vartheta_y}{\partial y}(x,y) = \frac{\frac{\partial^2\chi}{\partial y^2}(x,y)\cdot\left(\frac{\partial\chi}{\partial y}\right)_\perp(x,y)}{\|\frac{\partial\chi}{\partial y}(x,y)\|^2}\ . \tag{35}$$

In the following $\partial\rho_\alpha/\partial\alpha$ and $\partial\vartheta_\alpha/\partial\alpha$ are called α-stretch α-derivative and material α-curvature, respectively. For Piola's micro-macro identification the generalized coordinates of the discrete system are related to the functions χ and $\tilde{l}_\alpha^{\mu\nu}$ evaluated at $(x_i, y_j) = (i\varepsilon, j\varepsilon)$ as

$$\chi(x_i, y_j) = p_{i,j}\ ,\qquad \tilde{l}_\alpha^{\mu\nu}(x_i, y_j) = \tilde{l}_{(i,j),\alpha}^{\mu\nu}\ . \tag{36}$$

For the asymptotic identification, the energy (32) needs to be expanded in ε. The expansion of χ is given by

$$\chi(x_{i\pm1}, y_j) = \chi(x_i, y_j) \pm \varepsilon\frac{\partial\chi}{\partial x}(x_i, y_j) + \frac{\varepsilon^2}{2}\frac{\partial^2\chi}{\partial x^2}(x_i, y_j) + o(\varepsilon^2)\ ,$$
$$\chi(x_i, y_{j\pm1}) = \chi(x_i, y_j) \pm \varepsilon\frac{\partial\chi}{\partial y}(x_i, y_j) + \frac{\varepsilon^2}{2}\frac{\partial^2\chi}{\partial y^2}(x_i, y_j) + o(\varepsilon^2)\ . \tag{37}$$

Combining the asymptotic expansion (31) with (36)$_2$, $\tilde{l}_x^{\mu\nu}(x_{i\pm1}, y_j) = \tilde{l}_x^{\mu\nu}(x_i, y_j) + o(\varepsilon^0)$ and $\tilde{l}_y^{\mu\nu}(x_i, y_{j\pm1}) = \tilde{l}_y^{\mu\nu}(x_i, y_j) + o(\varepsilon^0)$, yields

$$l_{(i\pm1,j),x}^{\mu\nu} = \frac{1}{2\cos\gamma}\varepsilon + \tilde{l}_x^{\mu\nu}(x_i, y_j)\varepsilon^2 + o(\varepsilon^2)\ ,$$
$$l_{(i,j\pm1),y}^{\mu\nu} = \frac{1}{2\cos\gamma}\varepsilon + \tilde{l}_y^{\mu\nu}(x_i, y_j)\varepsilon^2 + o(\varepsilon^2)\ . \tag{38}$$

In order to further expand (32), the terms $\theta_{(i,j),\alpha}$, $\varphi_{(i,j),\alpha}^{\mu S} - \varphi_{(i,j),\alpha}^{\mu D}$ and $\xi_{(i,j),\alpha}^\mu$ need to be expanded up to first order (see App. 6). For $\theta_{(i,j),\alpha}$ according to (71)

$$\theta_{(i,j),\alpha} = \varepsilon\frac{\partial\vartheta_{(i,j),\alpha}}{\partial\alpha}(x_i, y_j) + o(\varepsilon)\ . \tag{39}$$

The differences $\varphi_{(i,j),\alpha}^{1(2)S} - \varphi_{(i,j),\alpha}^{1(2)D}$ are given by (78) as

$$\varphi_{(i,j),\alpha}^{1(2)S} - \varphi_{(i,j),\alpha}^{1(2)D} = \left.\frac{4[\rho_\alpha^2 - (1/2\cos^2\gamma)](\tilde{l}_\alpha^{1(2)S} - \tilde{l}_\alpha^{1(2)D}) + (1/\cos\gamma)\frac{\partial(\rho_\alpha^2)}{\partial\alpha} + (2/\cos^2\gamma)(\tilde{l}_\alpha^{2(1)D} - \tilde{l}_\alpha^{2(1)S})}{4\rho_\alpha(1/2\cos\gamma)\sqrt{(1/\cos^2\gamma) - \rho_\alpha^2}}\right|_{(x,y)=(x_i,y_j)}\varepsilon + o(\varepsilon)\ . \tag{40}$$

The angles $\xi_{(i,j),\alpha}^\mu$ are given by (80) as

$$\xi_{(i,j),\alpha}^\mu = \cos^{-1}\left(1 - \frac{\rho_\alpha^2}{1/2\cos^2\gamma}\right)\Bigg|_{(x,y)=(x_i,y_j)} + o(\varepsilon^0)\ . \tag{41}$$

Substituting (39), (40) and (41) into (32) together with $\rho_\alpha(x_i, y_j) = \|\frac{\partial \chi}{\partial \alpha}\|$, the desired expansion of the micro-model energy $\mathfrak{E}_\varepsilon$ is derived as a function of the kinematic descriptors χ and $\tilde{l}_\alpha^{\mu\nu}$ as

$$
\mathfrak{E}_\varepsilon = \sum_{i,j} \sum_\alpha \left\{ \frac{k_E \varepsilon^4}{2} \left[\sum_{\mu,\nu} (\tilde{l}_\alpha^{\mu\nu})^2 + o(\varepsilon^0) \right] + k_S \left[\cos^{-1}\left(1 - \frac{\rho_\alpha^2}{1/2\cos^2\gamma} \right) - \pi + 2\gamma + o(\varepsilon^0) \right]^2 \right\}_{(x,y)=(x_i,y_j)}
$$
$$
+ \sum_{i,j} \sum_\alpha \frac{k_F \varepsilon^2}{2} \left[\frac{\partial\vartheta}{\partial\alpha} + \frac{4[\rho_\alpha^2 - (1/2\cos^2\gamma)](\tilde{l}_\alpha^{1S} - \tilde{l}_\alpha^{1D}) + (1/\cos\gamma)\frac{\partial(\rho_\alpha^2)}{\partial\alpha} + (2/\cos^2\gamma)(\tilde{l}_\alpha^{2D} - \tilde{l}_\alpha^{2S})}{4\rho_\alpha(1/2\cos\gamma)\sqrt{(1/\cos^2\gamma) - \rho_\alpha^2}} + o(\varepsilon^0) \right]^2_{(x,y)=(x_i,y_j)}
$$
$$
+ \sum_{i,j} \sum_\alpha \frac{k_F \varepsilon^2}{2} \left[\frac{\partial\vartheta}{\partial\alpha} + \frac{4[\rho_\alpha^2 - (1/2\cos^2\gamma)](\tilde{l}_\alpha^{2S} - \tilde{l}_\alpha^{2D}) + (1/\cos\gamma)\frac{\partial(\rho_\alpha^2)}{\partial\alpha} + (2/\cos^2\gamma)(\tilde{l}_\alpha^{1D} - \tilde{l}_\alpha^{1S})}{4\rho_\alpha(1/2\cos\gamma)\sqrt{(1/\cos^2\gamma) - \rho_\alpha^2}} + o(\varepsilon^0) \right]^2_{(x,y)=(x_i,y_j)}.
$$
(42)

Let the parameters $K_E, K_F, K_S > 0$ be constants, which do not depend on ε. Then these constants are related to the stiffnesses of each discrete system with micro length scale ε by a scaling law

$$
k_E = K_E \varepsilon^{-2} , \qquad k_F = K_F , \qquad k_S = K_S \varepsilon^2 .
$$
(43)

2.4. Bi-pantographic fabrics – macro-model

The continuum limit is now obtained by letting $\varepsilon \to 0$ and considering the sum to turn into an integral according to $\sum_{i,j} f(x_i, y_j)\varepsilon^2 \xrightarrow{\varepsilon \to 0} \int_\Omega f \, dA$, where f is a real valued function defined on Ω. Using (42) together with the scaling law (43), the deformation energy for the homogenised macro-model becomes

$$
\mathfrak{E} = \int_\Omega \sum_\alpha \left\{ \frac{K_E}{2} \left[\sum_{\mu,\nu} (\tilde{l}_\alpha^{\mu\nu})^2 \right] + K_S \left[\cos^{-1}\left(1 - \frac{\rho_\alpha^2}{1/2\cos^2\gamma} \right) - \pi + 2\gamma \right]^2 \right\} dA
$$
$$
+ \int_\Omega \sum_\alpha \frac{K_F}{2} \left[\frac{\partial\vartheta_\alpha}{\partial\alpha} + \frac{4[\rho_\alpha^2 - (1/2\cos^2\gamma)](\tilde{l}_\alpha^{1S} - \tilde{l}_\alpha^{1D}) + (1/\cos\gamma)\frac{\partial(\rho_\alpha^2)}{\partial\alpha} + (2/\cos^2\gamma)(\tilde{l}_\alpha^{2D} - \tilde{l}_\alpha^{2S})}{4\rho_\alpha(1/2\cos\gamma)\sqrt{(1/\cos^2\gamma) - \rho_\alpha^2}} \right]^2 dA
$$
(44)
$$
+ \int_\Omega \sum_\alpha \frac{K_F}{2} \left[\frac{\partial\vartheta_\alpha}{\partial\alpha} + \frac{4[\rho_\alpha^2 - (1/2\cos^2\gamma)](\tilde{l}_\alpha^{2S} - \tilde{l}_\alpha^{2D}) + (1/\cos\gamma)\frac{\partial(\rho_\alpha^2)}{\partial\alpha} + (2/\cos^2\gamma)(\tilde{l}_\alpha^{1D} - \tilde{l}_\alpha^{1S})}{4\rho_\alpha(1/2\cos\gamma)\sqrt{(1/\cos^2\gamma) - \rho_\alpha^2}} \right]^2 dA .
$$

Considerations on the above derived continuum limit analogous to those made in the previous subsection dealing with preliminary computations can be invoked. The above deformation energy is objective and discrete floppy modes transfer to the continuum after homogenisation. The above deformation energy is vanishing for $\chi(x,y) = [x + (ay + b)x]e_x + [y + (cy + d)x]e_y$ [35] when $K_S = 0$. When $a = c = d = 0$, then χ represents uniform extension, while when $a = c = 0$ it describes uniform shear deformation, which is the only non-rigid zero energy deformation mode for pantographic fabrics, [11]. The derived continuum limit – as for pantographic fabrics – inherits its orthotropicity from its fibered structure at the micro-scale, i.e. it can be regarded as made by assembling two identical orthogonal families of (equispaced) parallel discrete pantographic beams. Let us now define the deformation energy density Ψ as the integrand of (44). For the energy to be stationary, the necessary conditions are obtained by equating to zero the variation of the deformation energy functional (44) with respect to admissible variations in the independent kinematic descriptors. First, only the variation with respect to $\tilde{l}_\alpha^{\mu\nu}$ is studied, and results in a linear system of eight algebraic equations given by $\partial\Psi/\partial\tilde{l}_\alpha^{\mu\nu} = 0$ in which $\tilde{l}_\alpha^{\mu\nu}$ are the unknowns. Introducing the notations

$$
C_1^\alpha = \frac{K_F}{2K_F\rho_\alpha^2 - 1/4\cos^2\gamma(K_E\rho_\alpha^2 + 8K_F)} , \qquad C_2^\alpha = \frac{K_F\sqrt{1/\cos^2\gamma - \rho_\alpha^2}}{K_E(1/4\cos^2\gamma)\rho_\alpha^2 - 2K_F\rho_\alpha^2 - 4K_E(1/16\cos^4\gamma)} ,
$$
(45)

necessary conditions for equilibrium are that

$$
\tilde{l}_\alpha^{\mu D} = \frac{1}{2\cos\gamma}\rho_\alpha \left[\frac{\partial\rho_\alpha}{\partial\alpha}C_1^\alpha + (-1)^{\mu-1}\frac{\partial\vartheta_\alpha}{\partial\alpha}C_2^\alpha \right] , \qquad \tilde{l}_\alpha^{\mu S} = \frac{1}{2\cos\gamma}\rho_\alpha \left[-\frac{\partial\rho_\alpha}{\partial\alpha}C_1^\alpha + (-1)^\mu\frac{\partial\vartheta_\alpha}{\partial\alpha}C_2^\alpha \right] .
$$
(46)

By substituting the results (46) into (44), a kinematic reduction is performed and results in the deformation energy functional of the bi-pantographic structure

$$
\mathfrak{E} = \int_\Omega \sum_\alpha \left\{ K_E K_F \left[\frac{\rho_\alpha^2 \cos^2\gamma - 1}{\rho_\alpha^2 \cos^2\gamma \left(K_E - 8K_F \cos^2\gamma\right) - K_E} \left(\frac{\partial\vartheta_\alpha}{\partial\alpha}\right)^2 \right. \right.
$$
$$
\left. \left. + \frac{\rho_\alpha^2 \cos^2\gamma}{\left(1 - \rho_\alpha^2 \cos^2\gamma\right)\left[8K_F + \rho_\alpha^2\left(K_E - 8K_F \cos^2\gamma\right)\right]} \left(\frac{\partial\rho_\alpha}{\partial\alpha}\right)^2 \right] + K_S \left[\cos^{-1}\left(1 - \frac{\rho_\alpha^2}{1/2\cos^2\gamma}\right) - \pi + 2\gamma \right]^2 \right\} dA
$$

(47)

which depends on the placement function χ only. Notice that, besides the term $\left(\frac{\partial\chi}{\partial\alpha}\right)_\perp \cdot \frac{\partial^2\chi}{\partial\alpha^2}$ being related to the material α-curvature $\frac{\partial\vartheta_\alpha}{\partial\alpha}$ by means of (35), also the term $\frac{\partial\chi}{\partial\alpha} \cdot \frac{\partial^2\chi}{\partial\alpha^2}$ appears which in turn is related to the α-stretch α-derivative $\frac{\partial\rho_\alpha}{\partial\alpha}$ given by equation (35).

A detailed derivation of Euler-Lagrange equations, essential and natural boundary conditions (BC's) as deduced from stationarity condition for energy functionals of the form $\int_\Omega W(\nabla\chi, \nabla\nabla\chi) dA$ – as that in (47) – is beyond the scope of this paper, and the reader is referred to [46]. However, it is worth recalling that in such a case non-classical essential normal placement gradient BC's – i.e. prescribing $\nabla\chi(x,y) \cdot n(x,y) = f(x,y)$ – can be given at boundaries $\partial\Omega_k$'s – n being the outwards pointing unit normal – and essential placement BC's – i.e. prescribing $\chi(x,y) = g(x,y)$ – can be given at vertices belonging to $[\partial\partial\Omega]$, in addition to classical essential placement BC's at boundaries $\partial\Omega_k$.

2.5. Bi-pantographic fabrics – linearisation of deformation energy

Let the vector valued displacement field u be defined by $u(x,y) = \chi(x,y) - xe_x - ye_y$. Then by the Piola's identification (36) and by the definition of nodal displacements $u_{i,j}$ we have $u(x_i, y_j) = u_{i,j}$. From Taylor expansions it follows that

$$
\vartheta_x = \tan^{-1}\left[\frac{\partial u}{\partial x} \cdot e_y \Big/ \left(1 + \frac{\partial u}{\partial x} \cdot e_x\right)\right] = \frac{\partial u}{\partial x} \cdot e_y + o\left(\left\|\frac{\partial u}{\partial x}\right\|\right) = o\left(\left\|\frac{\partial u}{\partial x}\right\|^0\right),
$$
$$
\vartheta_y = \tan^{-1}\left[\frac{\partial u}{\partial y} \cdot e_x \Big/ \left(1 + \frac{\partial u}{\partial y} \cdot e_y\right)\right] = \frac{\partial u}{\partial y} \cdot e_x + o\left(\left\|\frac{\partial u}{\partial y}\right\|\right) = o\left(\left\|\frac{\partial u}{\partial y}\right\|^0\right),
$$

(48)

and therefore

$$
\frac{\partial\vartheta_x}{\partial x} = \frac{\partial^2 u}{\partial x^2} \cdot e_y + o\left(\left\|\frac{\partial u}{\partial x}\right\|^0\right), \quad \frac{\partial\vartheta_y}{\partial y} = \frac{\partial^2 u}{\partial y^2} \cdot e_x + o\left(\left\|\frac{\partial u}{\partial y}\right\|^0\right).
$$

(49)

Moreover,

$$
\rho_x = \left[\left(1 + \frac{\partial u}{\partial x} \cdot e_x\right)^2 + \left(\frac{\partial u}{\partial x} \cdot e_y\right)^2\right]^{\frac{1}{2}} = 1 + \frac{\partial u}{\partial x} \cdot e_x + o\left(\left\|\frac{\partial u}{\partial x}\right\|\right) = 1 + o\left(\left\|\frac{\partial u}{\partial x}\right\|^0\right),
$$
$$
\rho_y = \left[\left(1 + \frac{\partial u}{\partial y} \cdot e_y\right)^2 + \left(\frac{\partial u}{\partial y} \cdot e_x\right)^2\right]^{\frac{1}{2}} = 1 + \frac{\partial u}{\partial y} \cdot e_y + o\left(\left\|\frac{\partial u}{\partial y}\right\|\right) = 1 + o\left(\left\|\frac{\partial u}{\partial y}\right\|^0\right),
$$

(50)

and thus

$$
\frac{\partial\rho_\alpha}{\partial\alpha} = \frac{\partial^2 u}{\partial\alpha^2} \cdot e_\alpha + o\left(\left\|\frac{\partial u}{\partial\alpha}\right\|^0\right).
$$

(51)

Hence, the energy (47) rewrites as (see equation (85) in App. A)

$$
\mathfrak{E} = \int_\Omega \left\{ \left[\frac{K_E K_F \cos^2\gamma}{(1 - \cos^2\gamma)\left[8K_F + K_E - 8K_F \cos^2\gamma\right]} \right] \left[\left(\frac{\partial^2 u}{\partial x^2} \cdot e_x\right)^2 + \left(\frac{\partial^2 u}{\partial y^2} \cdot e_y\right)^2 \right] \right\} dA
$$
$$
+ \int_\Omega \left\{ \left[\frac{K_E K_F(\cos^2\gamma - 1)}{\cos^2\gamma(K_E - 8K_F \cos^2\gamma) - K_E} \right] \left[\left(\frac{\partial^2 u}{\partial x^2} \cdot e_y\right)^2 + \left(\frac{\partial^2 u}{\partial y^2} \cdot e_x\right)^2 \right] \right\} dA
$$
$$
+ \int_\Omega \left\{ \sum_\alpha [4K_S \cot\gamma] \left(\frac{\partial u}{\partial\alpha} \cdot e_\alpha\right)^2 + o\left(\left\|\frac{\partial u}{\partial\alpha}\right\|^2\right) \right\} dA .
$$

(52)

For small strain hypothesis the remainder $o(\|\partial u/\partial\alpha\|^2)$ in equation (52) can be neglected.

3. Computational aspects

In this section, the problem to be solved is introduced and solution methodologies employed for the macro- and micro-model are briefly recalled.

3.1. Boundary value problem (non-standard bias extension test)

A rectangular specimen, i.e. $N_\Omega = 4$, with sides $L =$187 mm $\times$ $\ell =$119 mm and $\varepsilon=$12.02 mm is considered, see Fig. 3. The geometric parameter γ is assumed to be equal to $\pi/6$. The following essential boundary conditions are considered

$$u(x,y) = 0 \text{ at } (x,y) \in \partial\Omega_1 , \qquad\qquad u(x,y) = \bar{u}e_\zeta \text{ at } (x,y) \in \partial\Omega_3, \ \bar{u} \in \mathbb{R}$$
$$[\nabla u(x,y)]n(x,y) = 0 \text{ at } (x,y) \in \partial\Omega_1 , \qquad [\nabla u(x,y)]n(x,y) = 0 \text{ at } (x,y) \in \partial\Omega_3 \tag{53}$$

which do not entail a floppy deformation mode. As the displacement field $u(x,y)$ is enforced to be constant along the boundaries $\partial\Omega_1$ and $\partial\Omega_3$, then $[\nabla u(x,y)]n_\perp(x,y)$ is also vanishing along those boundaries. This, together with $(53)_2$, implies that

$$\nabla u(x,y) = 0 \text{ at } (x,y) \in \partial\Omega_1 \cup \partial\Omega_3 . \tag{54}$$

Equation (54) is equivalent to

$$\rho_\alpha(x,y) = 1 \text{ at } (x,y) \in \partial\Omega_1 \cup \partial\Omega_3 , \qquad \vartheta_\alpha(x,y) = 0 \text{ at } (x,y) \in \partial\Omega_1 \cup \partial\Omega_3. \tag{55}$$
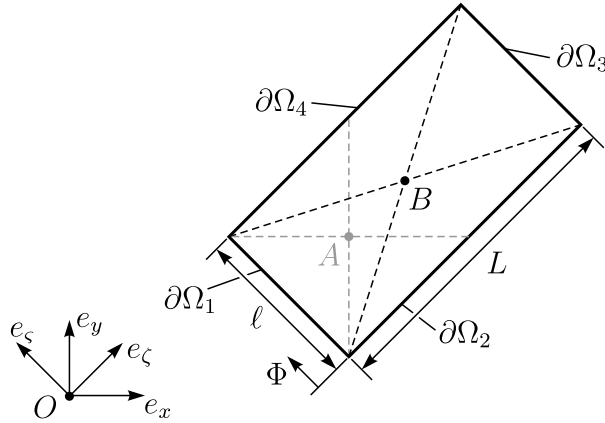

FIGURE 3. Schematic drawing of the reference domain Ω considered in the boundary value problem for the macro-model.

To compare the micro- and macro-model, beyond the micro-macro identification (12), the following micro-macro correspondences – based on neglecting non-leading ε-terms in Taylor expansions of continuum quantities evaluated at discrete points – shall be taken into account. For stretches and orientations of pantographic beams

$$\rho_x (x_i, y_i) \leftrightarrow \frac{\|p_{i+1,j} - p_{i,j}\|}{\varepsilon} , \qquad \vartheta_x (x_i, y_j) \leftrightarrow \vartheta_{i,j} = \tan^{-1}\left[\frac{(p_{i,j} - p_{i-1,j}) \cdot e_y}{(p_{i,j} - p_{i-1,j}) \cdot e_x}\right]$$
$$\rho_y (x_i, y_j) \leftrightarrow \frac{\|p_{i,j+1} - p_{i,j}\|}{\varepsilon} , \qquad \vartheta_y (x_i, y_j) \leftrightarrow \vartheta_{i,j} = \tan^{-1}\left[\frac{(p_{i,j} - p_{i,j-1}) \cdot e_x}{(p_{i,j} - p_{i,j-1}) \cdot e_y}\right] . \tag{56}$$

In addition, the micro-strains $\tilde{l}_\alpha^{\mu\nu}$ are related by

$$\tilde{l}_\alpha^{\mu\nu}(x_i, y_j) \leftrightarrow \frac{l_{(i,j),\alpha}^{\mu\nu}}{\varepsilon} . \tag{57}$$

The deformation energy density $\Psi(x,y)$, which is the integrand of (47), is compared by the following relation

$$\Psi(x_i, y_j) \leftrightarrow \Psi_{i,j} . \tag{58}$$

The shear angle is compared by the following relation

$$\left[\pi/2 - \arccos\left(\frac{\nabla\chi \, e_x \cdot \nabla\chi \, e_y}{\|\nabla\chi \, e_x\|\|\nabla\chi \, e_y\|}\right)\right]_{(x,y)=(x_i,y_j)} \leftrightarrow \pi/2 - \arccos\left[\frac{(p_{i+1,j} - p_{i,j}) \cdot (p_{i,j+1} - p_{i,j})}{\|p_{i+1,j} - p_{i,j}\|\|p_{i,j+1} - p_{i,j}\|}\right] . \tag{59}$$

micro-model	macro-model
$u_{i,j} = 0$ for all (i,j) s.t. $(x_i, y_j) \in \partial\Omega_1$ $u_{i,j} = \bar{u}e_\zeta$ for all (i,j) s.t. $(x_i, y_j) \in \partial\Omega_3$	$u(x,y) = 0$ for all $(x,y) \in \partial\Omega_1$ $u(x,y) = \bar{u}e_\zeta$ for all $(x,y) \in \partial\Omega_3$
$u_{i+1,j} = u_{i,j}$ for all (i,j) s.t. $(x_i, y_j) \in \partial\Omega_1$ $u_{i,j+1} = u_{i,j}$ for all (i,j) s.t. $(x_i, y_j) \in \partial\Omega_1$ $u_{i-1,j} = u_{i,j}$ for all (i,j) s.t. $(x_i, y_j) \in \partial\Omega_3$ $u_{i,j-1} = u_{i,j}$ for all (i,j) s.t. $(x_i, y_j) \in \partial\Omega_3$	$[\nabla u(x,y)]n(x,y) = 0$ for all $(x,y) \in \partial\Omega_1 \cup \Omega_3$

TABLE 1. Boundary conditions for micro- and macro-model.

Last, in an analogous fashion the following micro-macro correspondences are defined on boundaries

$$\frac{\partial u}{\partial x}(x_i, y_j) \leftrightarrow \frac{u_{i+1,j} - u_{i,j}}{\varepsilon} \text{ and } \frac{\partial u}{\partial y}(x_i, y_j) \leftrightarrow \frac{u_{i,j+1} - u_{i,j}}{\varepsilon} \text{ for all } (x_i, y_j) \in \partial\Omega_1$$

$$\frac{\partial u}{\partial x}(x_i, y_j) \leftrightarrow \frac{u_{i,j} - u_{i-1,j}}{\varepsilon} \text{ and } \frac{\partial u}{\partial y}(x_i, y_j) \leftrightarrow \frac{u_{i,j} - u_{i,j-1}}{\varepsilon} \text{ for all } (x_i, y_j) \in \partial\Omega_3$$

(60)

which, together with Piola's micro-macro identification (36), are used to establish a correspondence between boundary conditions (53) for the continuum model and those for the discrete one. Such a correspondence is reported in Tab. 1.

3.2. Macro-model – Finite Element formulation

A mixed finite element formulation is adopted for the solution of the macro-model. Let us define the following augmented energy functional

$$\tilde{\mathfrak{E}} = \sum_{k=1}^{N_\Omega} \int_{\partial\Omega_k} \sum_\alpha \left\{ \mu_\alpha \cdot [(\nabla u - M)\, n_\perp] \right\} \mathrm{d}A + \int_\Omega \sum_\alpha \left\{ \lambda_\alpha \cdot \left(Me_\alpha - \frac{\partial u}{\partial \alpha} \right) + K_E K_F \left[\frac{(\rho_\alpha^2 \cos^2 \gamma - 1)[\kappa_\alpha(M)]^2}{\rho_\alpha^2 \cos^2 \gamma \, (K_E - 8K_F \cos^2 \gamma) - K_E} \right. \right.$$

$$\left. + \frac{(\rho_\alpha^2 \cos^2 \gamma)[\iota_\alpha(M)]}{(1 - \rho_\alpha^2 \cos^2 \gamma)\,[8K_F + \rho_\alpha^2\,(K_E - 8K_F \cos^2 \gamma)]} \right] + K_S \left[\cos^{-1}\left(1 - \frac{\rho_\alpha^2}{1/2\cos^2 \gamma}\right) - \pi + 2\gamma \right]^2 \right\} \mathrm{d}A$$

$$+ \int_{\partial\Omega_1 \cup \partial\Omega_3} (\eta \cdot [\nabla u]n)\mathrm{d}l + \int_{\partial\Omega_1} (\gamma \cdot u)\,\mathrm{d}l + \int_{\partial\Omega_3} [\upsilon \cdot (u - \bar{u}e_\zeta)]\,\mathrm{d}l \,.$$

(61)

where M is an independent auxiliary field that is weakly enforced by Lagrange multipliers μ_α and λ_α to be equal to ∇u [47], and

$$\kappa_x(M) = \frac{\frac{\partial(Me_x)}{\partial x} \cdot [(1 + \frac{\partial u}{\partial x} \cdot e_x, \frac{\partial u}{\partial x} \cdot e_y)^\mathsf{T}]_\perp}{\|(1 + \frac{\partial u}{\partial x} \cdot e_x, \frac{\partial u}{\partial x} \cdot e_y)^\mathsf{T}\|^2} \,, \qquad \iota_x(M) = \frac{\frac{\partial(Me_x)}{\partial x} \cdot (1 + \frac{\partial u}{\partial x} \cdot e_x, \frac{\partial u}{\partial x} \cdot e_y)^\mathsf{T}}{\|(1 + \frac{\partial u}{\partial x} \cdot e_x, \frac{\partial u}{\partial x} \cdot e_y)^\mathsf{T}\|}$$

$$\kappa_y(M) = \frac{\frac{\partial(Me_y)}{\partial y} \cdot [(1 + \frac{\partial u}{\partial y} \cdot e_y, \frac{\partial u}{\partial y} \cdot e_x)^\mathsf{T}]_\perp}{\|(1 + \frac{\partial u}{\partial y} \cdot e_y, \frac{\partial u}{\partial y} \cdot e_x)^\mathsf{T}\|^2} \,, \qquad \iota_y(M) = \frac{\frac{\partial(Me_y)}{\partial y} \cdot (1 + \frac{\partial u}{\partial y} \cdot e_y, \frac{\partial u}{\partial y} \cdot e_x)^\mathsf{T}}{\|(1 + \frac{\partial u}{\partial y} \cdot e_y, \frac{\partial u}{\partial y} \cdot e_x)^\mathsf{T}\|}$$

(62)

are α-curvature (κ_α) and α-stretch α-derivative (ι_α) expressed in terms of only first spatial derivatives of the independent fields u and M. In such a way, the deformation energy (47) can be transformed into an augmented energy functional written in terms of first spatial derivatives of the independent kinematic quantities. The discretisation of these quantities by the finite element method to solve the stationarity condition of such augmented energy functional does not require C^1-continuous shape functions like those needed to solve the stationarity condition for the energy (47) in terms of the only unknown field u. Let $\tilde{\Psi}$ be the argument of integration over Ω in (61). Let $\tilde{\Psi}_k$ be the argument of integration over $\partial\Omega_k$ in (61). From the stationarity condition for the energy (61) is determined the weak form

$$0 = \sum_\alpha \sum_{k=1}^{N_\Omega} \int_{\partial\Omega_k} \left[\frac{\partial \tilde{\Psi}_k}{\partial (\partial u/\partial \alpha)} \cdot \delta\left(\frac{\partial u}{\partial \alpha}\right) + \frac{\tilde{\Psi}_k}{\partial(Me_\alpha)} \cdot \delta(Me_\alpha) + \frac{\partial \tilde{\Psi}_k}{\partial \mu_\alpha} \cdot \delta\mu_\alpha \right] \mathrm{d}l$$

$$+ \sum_\alpha \int_\Omega \left[\frac{\partial \tilde{\Psi}}{\partial (\partial u/\partial \alpha)} \cdot \delta\left(\frac{\partial u}{\partial \alpha}\right) + \frac{\partial \tilde{\Psi}}{\partial(Me_\alpha)} \cdot \delta(Me_\alpha) + \frac{\partial \tilde{\Psi}}{\partial \lambda_\alpha} \cdot \delta\lambda_\alpha \right] \mathrm{d}A + \sum_{k=1}^{N_\Omega} \int_{\partial\Omega_k} \left[\frac{\partial \tilde{\Psi}_k}{\partial \eta} \cdot \delta\eta + \frac{\partial \tilde{\Psi}_k}{\partial \gamma} \cdot \delta\gamma + \frac{\partial \tilde{\Psi}_k}{\partial \upsilon} \cdot \delta\upsilon \right] \mathrm{d}l$$

(63)

where $\delta(\cdot)$ denotes the kinematically admissible variation of $(\cdot)$, which can then be solved numerically by a finite element code. The *weak form* package of the software COMSOL Multiphysics, which implements standard finite element techniques [48, 49], was used for the discretisation and the subsequent solution procedure. Essential boundary conditions in equation (53) were not encoded within the basis functions but enforced by additional Lagrange multipliers (i.e. η_α, γ and υ in equation (61)). In such a mixed formulation, normal displacement gradient line-boundary conditions $(53)_2$ are enforced in terms of the auxiliary field M, while displacement line-boundary conditions $(53)_1$ are enforced in terms of the field u. Quadratic Lagrangian polynomials were used as basis functions for the fields χ and M. All Lagrange multiplier fields were discretised by linear Lagrange polynomials. The mesh was Delaunay tessellated with maximum diameter size equal to 8.45 mm (see Fig. 3). Energy convergence of the solutions was successfully checked for the mesh-size tending to 0. Solution of each step − i.e. for each $\bar{u}$ − was initialized by the solution of the previous one, considering for $\bar{u}$ a constant step-size $\Delta\bar{u}$ equal to 1 mm.

4. Materials and methods

4.1. Manufacturing

Specimens were 3D-printed using a Selective Laser Sintering (SLS) procedure. Polyamide powder was used as raw material. Possible use of metallic powders is to be investigated [50, 51, 52]. A picture obtained by optical microscopy showing the granularity of the printed Polyamide is presented in Fig. 4. Modelling at lower scales taking into account such a granular structure [53, 54, 55, 56] might be considered in future investigations.

FIGURE 4. Micrograph of a monolithic slender element of the prototype showing granularity of printed Polyamide.

All specimens were designed in SolidWorks Computer Aided Design (CAD) software by sketching 2D profiles and then using methods like extruding and lofting in order to produce solid shapes, see the technical drawings in Figs. 5, 6 and 10 (right). A full top-view of the manufactured specimen is shown in Fig. 7. The blue/red rotational springs in Fig. 2(c) and the adjacent extensional ones are fabricated as a whole by means of monolithic slender elements that are meant to predominantly bend (rotational spring) and (to a lesser extent) extend (extensional springs) in plane. Such elements are combined at extreme points by cylinders, which are meant to reproduce the green rotational springs of Fig. 2(c) by mainly twisting, and at middle points by hinge connections. They are shown in Fig. 8 (actual manufacturing on the left − A − and CAD modelling on the right − B). As assumed above, the angle γ is equal to $\pi/6$, see Fig. 10 (right).

Each pantographic beam is made of two families of monolithic slender elements forming an angle 2γ and lying onto two different parallel planes. The two families of pantographic beams (whose centrelines form an angle of 90°) lying onto two different planes are hinge connected at intersection points, which is at the mid-point of the monolithic slender elements. The structure is then doubled in the out-of-plane direction by reflection to avoid noticeable out-of-plane movements, making it symmetric with respect to its middle plane, see Fig. 5 (bottom). Hinge axes are monolithic elements running through the full out-of-plane length of the structure.

Hard-device conditions given in row three and six of Tab. 1 are obtained by connecting the adjacent hinge axes in proximity of the gripping areas, see Fig. 9, with stocky rhomboidal elements, meant to be rigid with respect to other elements of the specimen for the considered load range.

4.2. Testing and data acquisition

An MTS Tytron 250 testing-device was used for the experiments. The total reaction-force was measured by a device-own load cell, which is able to record axial forces in a range of ±250 N with an accuracy of 0.2 percent. Increasing displacements were prescribed horizontally on the right side of the specimen with a loading rate of 15 mm/min. The cross-head displacement was measured and monitored by a device-own encoder unit. Almost frictionless movement of the machine shaft was achieved by using an air-film-bearing. External vibrations were avoided by placing the system on a massive concrete-substructure. Pictures of the surface during deformations were taken (0.5 pictures/second) by
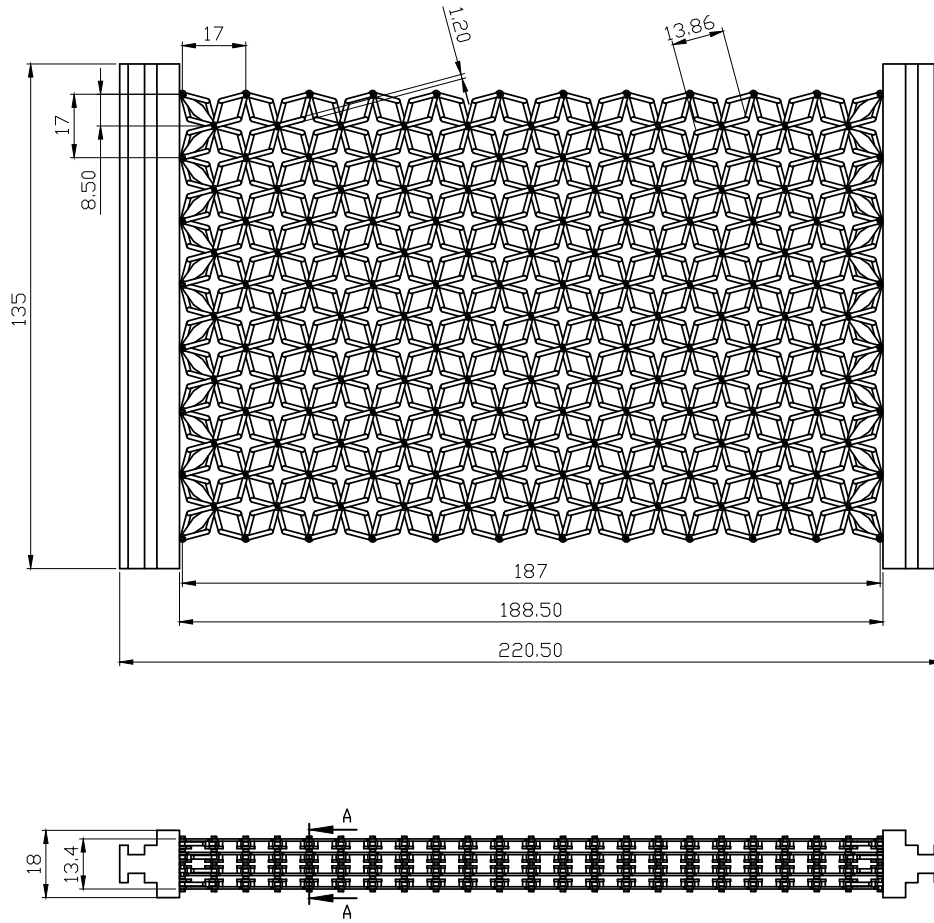
FIGURE 5. Technical drawing of the designed bi-pantographic prototypes. Top-view (top) and profile view (bottom). All lengths are expressed in mm.
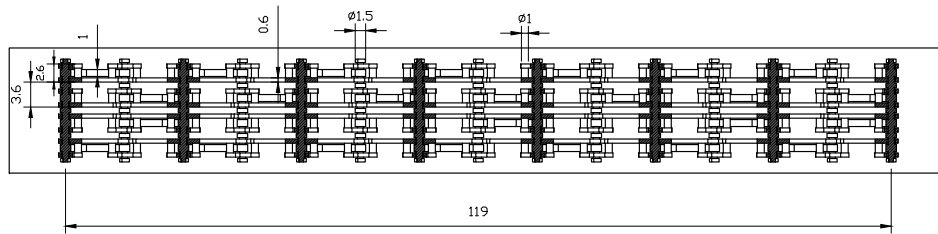

FIGURE 6. Section A-A indicated in Fig. 5 (bottom). All lengths are expresses in mm.

means of a Canon EOS 600D camera with a definition of 4272×2848 pixels. Each picture was synchronized with the recorded force-displacement data in real time. Regarding frictional dissipation due to PA2200 powder stuck in hinges, four loading-unloading cycles were performed for maximum prescribed displacements equal to 10 mm, 20 mm, 30 mm, 40 mm, and 50 mm, respectively. No out-of-plane movements of the specimen was observed. For all cycles, residual (negative compression) total reaction force following unloading was less than two percent of the total reaction force peak. Fig. 10(A) shows a picture of the deformed specimen.

4.3. Digital Image Correlation

The kinematic results described in the sequel were obtained via Digital Image Correlation (DIC). Digital Image Correlation consists in measuring displacement fields by registering pictures acquired during mechanical tests [57, 58, 59]. Various approaches have been introduced, namely, local (i.e. subset-based) analyses [60, 61, 62], and global (e.g. finite element based) techniques [63, 64, 65]. When dealing with pantographic structures, finite element based analyses have recently been performed at macroscopic [66] and mesoscopic scales [67]. In the present case, the sought
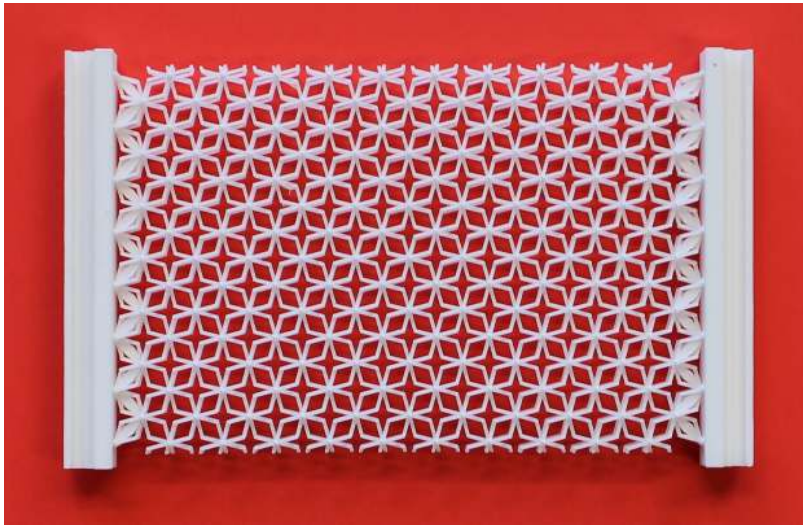
FIGURE 7. Full top-view of bi-pantographic prototype manufactured according to the technical drawings in Figs. 5, 6 and 10 (right).

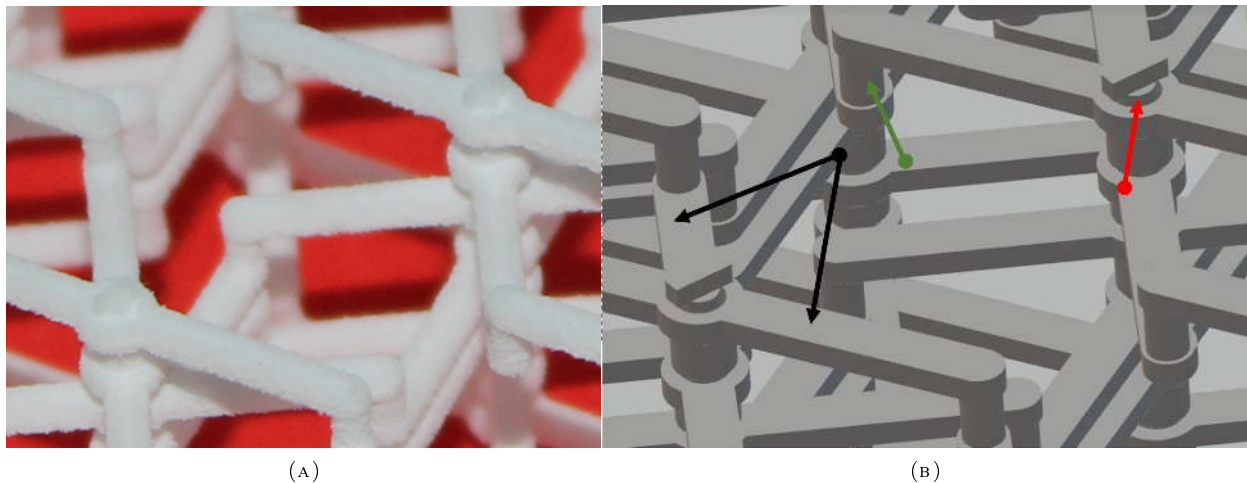(A)   (B)

FIGURE 8. Manufactured specimen (A) and CAD design (B). Zoomed view of 1. monolithic slender elements corresponding – by means of bending and extension – to blue/red rotational springs and to the adjacent extensional springs of Fig. 2(c) (black arrows), 2. cylinders materialising – by means of torsion – the green rotational springs of Fig. 2(c) (green arrow), and 3. hinges connecting monolithic slender elements at middle points (red arrow).

kinematics corresponds to the in-plane displacements of the hinges at positions $p_{i,j}$ of the bi-pantographic structure. The analysis of the displacement of these discrete points is performed via local DIC, i.e. using zones of interest or ZOIs [68] centred on each hinge. The simplest approach seeks the rigid body translation of each considered ZOI, as originally performed in particle image velocimetry [69, 70, 71, 72, 73]. Let f and g be the initial and current gray level images, respectively. For each ZOI, the correlation product

$$T(u) = \text{Argmax}_v \sum_{\text{ZOI}} f(x,y)g(x + v \cdot e_x, y + v \cdot e_y) \tag{64}$$

is maximized with respect to the rigid body translations $v \in \mathbb{R}^2$. The computation of the correlation product can be performed in Fourier space (thanks to the shift/modulation property) via FFTs to speed up the calculations [74]. No subpixel resolution [68] was sought in the present case since the expected displacements were very large when expressed in terms of pixels. Further, to account for the local angular variations between the beams connected by the hinges, the DIC calculations were performed incrementally, namely, for a series of pictures, the deformed picture

FIGURE 9. Realization of boundary conditions listed in Tab. 1. Manufactured specimen (A) and zoomed view of its CAD design (B).
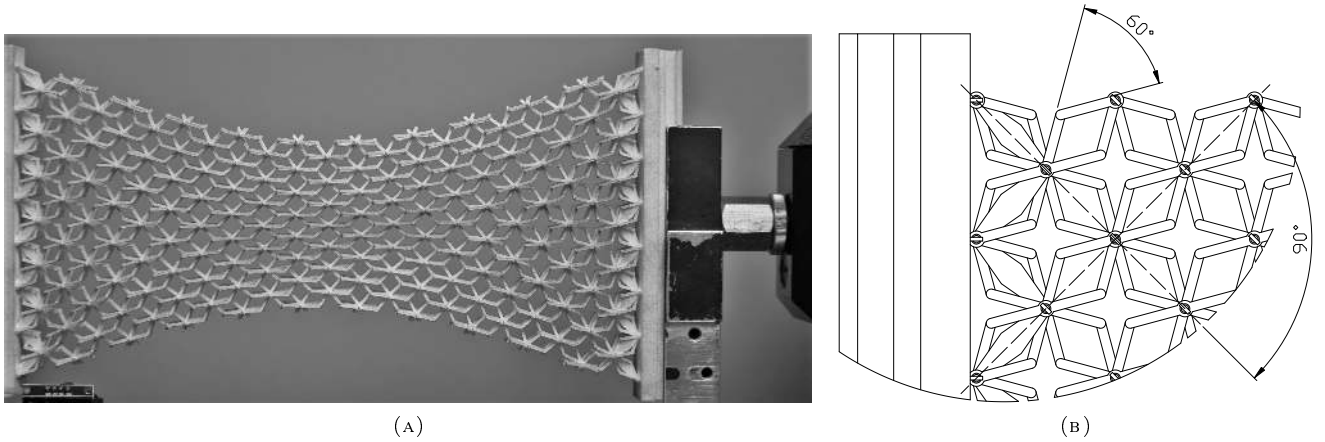

FIGURE 10. Deformed specimen (A) and zoomed view (B) of the top-left corner of Fig. 5 (top).

of the n-th registration step becomes the reference picture of the $n+1$-th step, and the corresponding displacement increment is cumulated with the previous ones to provide a Lagrangian estimation of the hinge displacements. Last, for each analysis, two passes were performed. The first one used a rather large ZOI size (i.e. 100×100 pixels) to get a robust first estimate. The second one utilised a smaller size (i.e. 50×50 pixels) to focus on the kinematic analysis about each hinge.

5. Results

The focus of this section is to present results obtained by the continuum model, and discuss how much they deviate from the experimental data. Owing to symmetry arguments (i.e. $D4$ [3] symmetry with respect to pantographic beam directions, symmetry of the specimen and boundary conditions with respect to specimen's axes) it is concluded that the following symmetries should be fulfilled by the continuum solution (analogous statements can be done for the discrete one) with the notation $g(\zeta, \varsigma)$ standing for $g[x(\zeta, \varsigma), y(\zeta, \varsigma)]$

$$
\begin{aligned}
\vartheta_y(\zeta, \varsigma) &= \vartheta_x(\zeta, \ell - \varsigma), & \rho_y(\zeta, \varsigma) &= \rho_x(L - \zeta, \varsigma) \\
\rho_y(\zeta, \varsigma) &= \rho_x(\zeta, \ell - \varsigma), & \vartheta_y(\zeta, \varsigma) &= \vartheta_x(L - \zeta, \varsigma)
\end{aligned}
\tag{65}
$$

and

$$
\vartheta_y(\zeta, \varsigma) = \vartheta_y(L - \zeta, \ell - \varsigma), \qquad \rho_y(\zeta, \varsigma) = \vartheta_y(L - \zeta, \ell - \varsigma) .
\tag{66}
$$

As in the considered problem either $0 < \vartheta_x(x,y) < \pi/2$ and $-\pi/2 < \vartheta_y(x,y) < 0$ or $0 < \vartheta_y(x,y) < \pi/2$ and $-\pi/2 < \vartheta_x(x,y) < 0$ – this can be seen a posteriori by looking at Fig. 14) – then the shear angle, which is null in the undeformed configuration and objective, is written in an easier way as $\pi/2 - |\vartheta_x| - |\vartheta_y|$. An analogous observation holds for the micro-model.

The maximum prescribed displacement $\bar{u}$ directed along ζ is equal to 50 mm. Parameters for the continuum (K_F, K_E and K_S) were found by fitting three-curves (see Fig. 11 and cf. also [11] where the same quantities – although defined for pantographic fabrics – were used for fitting). The first one (Fig. 11 (left)) is the total reaction force along the direction ζ (determined by the load cell of the testing machine) vs $\bar{u}$ (determined by the machine encoder unit). The second one (Fig. 11 (centre)) is the shear angle at pt. A (determined by DIC, see Fig. 3) vs $\bar{u}$. Finally, the third one (Fig. 11 (right)) is the shear angle at pt. B (determined by DIC, see Fig. 3) vs $\bar{u}$. The total reaction force acting on Ω_3 has been found for the continuum model by means of Castigliano's Theorem.

In order to check that computed Lagrange multipliers were consistent with the reaction force found by such a theorem, i.e. with energy conservation, one can compute the total reaction force acting on Ω_3 with the Lagrange multipliers as

$$-\int_{\Omega_3} \upsilon \cdot \zeta \, \mathrm{d}l. \tag{67}$$

This fact holds true for the numerical solution. Figure 12 compares the total reaction force along the direction ζ – as computed by the continuum model using Lagrange multipliers and Castigliano's theorem – vs $\bar{u}$. The forward finite difference approximation of $\partial\mathcal{E}/\partial\bar{u}$ was computed with a step size for $\bar{u}$ equal to $\Delta\bar{u} = 1$ mm. It is concluded that, up to finite difference discretization errors, the results obtained with the two methodologies are consistent. Owing to symmetry arguments, the total reaction force along the direction ς as computed with Lagrange multipliers should be cancelling out. Also this fact holds true for the numerical solution.
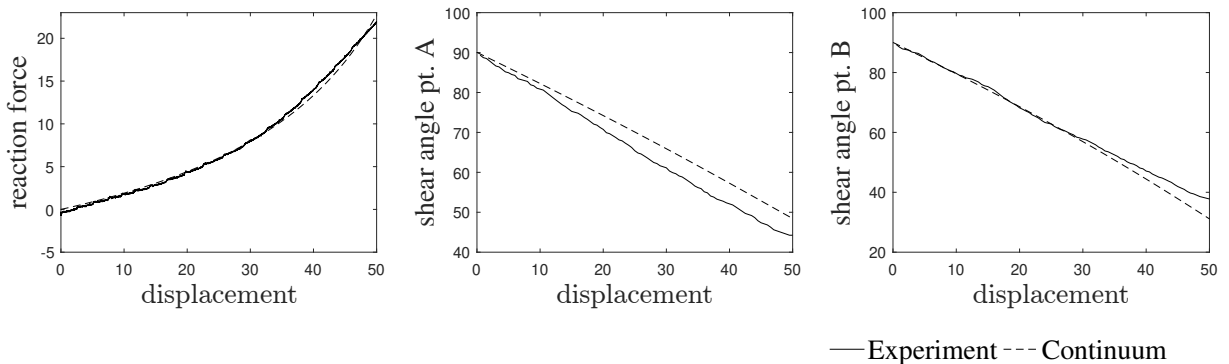

——Experiment ---Continuum

FIGURE 11. Total reaction force along the direction ζ with changed sign (N) vs prescribed displacement $\bar{u}$ (mm) along the direction e_ζ (left), shear angle at pt. A (°) vs prescribed displacement $\bar{u}$ (mm) along the direction e_ζ (centre), and shear angle (°) at pt. B vs prescribed displacement $\bar{u}$ (mm) along the direction e_ζ (right).

The fitted values of the parameters for the continuum model are $K_F = 0.9$ J, $K_E = 0.33$ J, $K_S = 34$ N·m^{-1}. Hence, the continuum model is capable to describe the considered experimental curves with only three constitutive parameters. The computed deformed configuration, i.e. $\chi(x_i, y_j)$, is compared for different prescribed $\bar{u}$ levels with experimentally measured data in Fig. 13. It is seen that experimental measurements by DIC and the continuum model agree very well. Experimental data, unlike the continuum model, exhibit a non-symmetry which is especially evident for $\bar{u} = 40$ mm and $\bar{u} = 50$ mm on the left. It is worth noting that only the use of homogenisation starting from a discrete model – with a target model not chosen a priori – allows such complex deformation energy to be recovered. The underlying family of discrete systems does not only lead to the deformation energy but also allows for a clear interpretation of non-standard boundary conditions that appear in this formulation.
Contour plots of the y-stretch ρ_y are shown in Fig. 14 for the continuum model. Figure 14 shows that the stretch is remarkably non-localized. This is due to pantographic beams being complete second gradient continua.

Let us quantify the sensitivity of the numerical simulation with respect to the application of non-standard zero normal displacement gradient boundary condition $[\nabla u(x,y)]n(x,y) = 0$ on $\Omega_1 \cup \Omega_3$. In Fig. 15, the quantities ρ_y and ϑ_y are plotted as functions of the local abscissa Φ of the boundary Ω_1 for the continuum model in both cases when zero normal displacement gradient boundary conditions are enforced and when they are not ($\bar{u} = 50$ mm). Especially
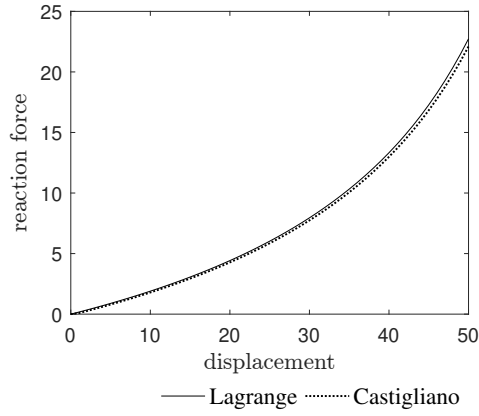
FIGURE 12. Total reaction force along the direction ζ with changed sign (N) vs $\bar{u}$ (mm) as computed by the continuum model using Lagrange multipliers and Castigliano's theorem. The forward finite difference approximation of $\partial \mathcal{E} / \partial \bar{u}$ has been computed with a step size for $\bar{u}$ equal to $\Delta \bar{u} = 1$ mm.
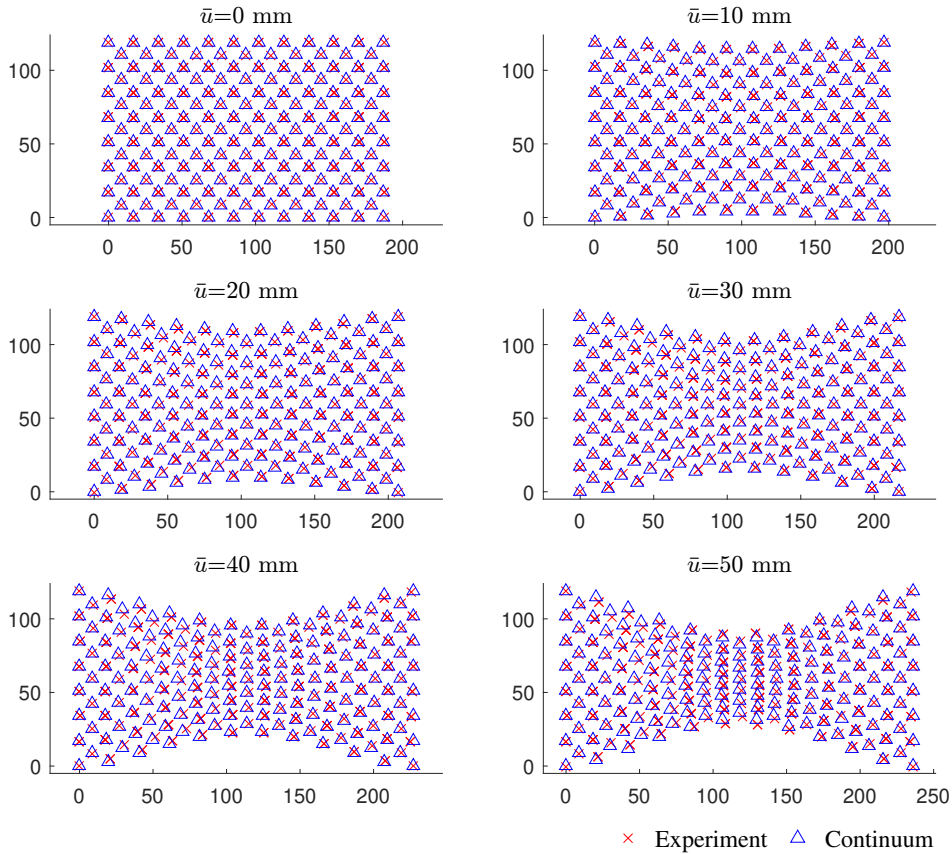

FIGURE 13. The deformed configuration as computed by the continuum model, i.e. $\chi(x_i, y_j)$, is compared for different applied $\bar{u}$ with experimental measurements. Abscissas and ordinates are expressed in mm.

in the vicinity of vertices of the domain Ω, the solution is strongly sensitive to the application of non-standard boundary conditions.
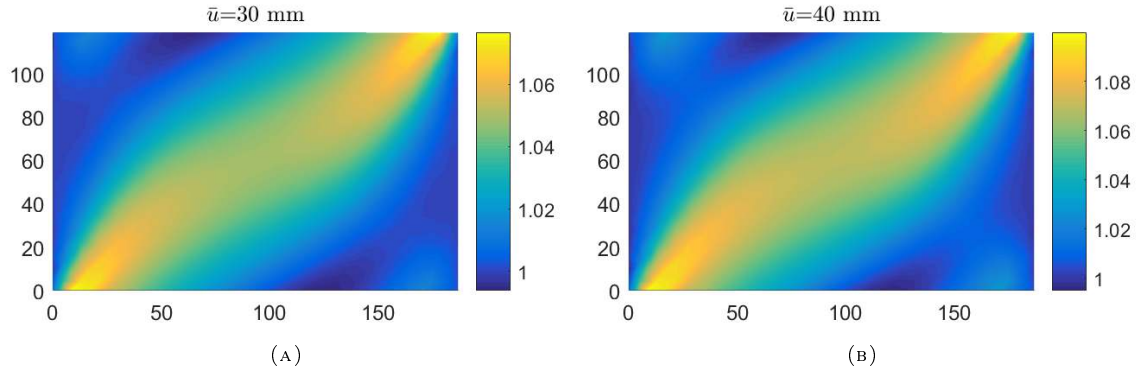
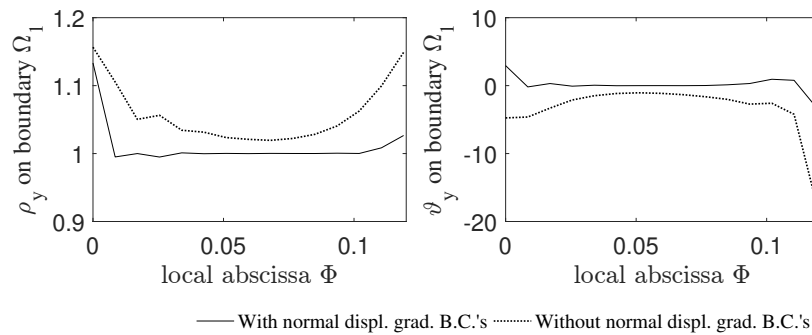FIGURE 14. y-stretch ρ_y as computed by the continuum model. Abscissas and ordinates are expressed in mm.

FIGURE 15. Plots of ρ_y (left) and of ϑ_y ($°$, right) vs the local abscissa Φ (m) of the boundary Ω_1 for continuum modelling when $\bar{u} = 50$ mm. The (arc-length) abscissa Φ is introduced in Fig. 3.

6. Conclusion and outlook

Bi-pantographic fabrics proved to have an extremely wide elastic range. This is possible because in such structures the total deformation is much greater than single-elastic-element deformations. Compatibly with boundary conditions and internal connection constraints, the elements arrange so as to minimize the total deformation energy by mimicking the wide variety of mechanisms corresponding to floppy modes.

Some future outlooks of the present work are

- designing, experimenting and analysing a bi-pantographic system obeying the discrete model with $k_S = 0$, which would mean that all cylinders connecting slender monolithic elements would be replaced by hinges, giving a purely second gradient material at macro-scale
- studying the dynamics of bi-pantographic fabrics, which could be done by exploiting the results already obtained for pantographic beams [75]
- studying out-of-plane deformations [76] of such metamaterials.

Acknowledgements. Authors thank P. Seppecher, G. Ganzosch and T. Lekszycki for stimulating discussions.

Appendix A

The terms θ_i and $\varphi_i^{\mu S} - \varphi_i^{\mu D}$ are expanded up to first order by using the definitions (1) and (3) together with the expansions (13) and (14). According to (12) and (13) the vectors between two adjacent points p_i are

$$p_{i+1} - p_i = \varepsilon \left[\chi'(s_i) + \frac{\varepsilon}{2} \chi''(s_i) + o(\varepsilon) \right] , \qquad p_i - p_{i-1} = \varepsilon \left[\chi'(s_i) - \frac{\varepsilon}{2} \chi''(s_i) + o(\varepsilon) \right] . \tag{68}$$

The arguments of $\tan^{-1}$ in (3) are written as functions of ε

$$
\begin{aligned}
h_{i+1}(\varepsilon) &= \frac{(p_{i+1} - p_i) \cdot e_y}{(p_{i+1} - p_i) \cdot e_x} \overset{(68)_1}{=} \frac{\chi'(s_i) \cdot e_y + \frac{\varepsilon}{2}\chi''(s_i) \cdot e_y + o(\varepsilon)}{\chi'(s_i) \cdot e_x + \frac{\varepsilon}{2}\chi''(s_i) \cdot e_x + o(\varepsilon)} \,, \\
h_i(\varepsilon) &= \frac{(p_i - p_{i-1}) \cdot e_y}{(p_i - p_{i-1}) \cdot e_x} \overset{(68)_2}{=} \frac{\chi'(s_i) \cdot e_y - \frac{\varepsilon}{2}\chi''(s_i) \cdot e_y + o(\varepsilon)}{\chi'(s_i) \cdot e_x - \frac{\varepsilon}{2}\chi''(s_i) \cdot e_x + o(\varepsilon)} \,.
\end{aligned}
\tag{69}
$$

It is noted that $h_i(0) = h_{i+1}(0) = [\chi'(s_i) \cdot e_y] / [\chi'(s_i) \cdot e_x]$. Moreover

$$
\begin{aligned}
h'_{i+1}(0) = -h'_i(0) &= \left. \frac{1}{2[\chi' \cdot e_x]^2} \left[(\chi'' \cdot e_y)(\chi' \cdot e_x) - (\chi'' \cdot e_x)(\chi' \cdot e_y) \right] \right|_{s=s_i} \\
&= \left. \frac{1}{2[\chi' \cdot e_x]^2} \chi'' \cdot (e_y \otimes e_x - e_x \otimes e_y) \cdot \chi' \right|_{s=s_i} = \frac{\chi''(s_i) \cdot \chi'_\perp(s_i)}{2\left[\chi'(s_i) \cdot e_x\right]^2} \,.
\end{aligned}
\tag{70}
$$

For a real valued function $h(\varepsilon)$, $\tan^{-1}(h(\varepsilon)) = \tan^{-1}(h(0)) + \frac{h'(0)}{1+h(0)^2}\varepsilon + o(\varepsilon)$. Since $h_i(0) = h_{i+1}(0)$, the first terms in the Taylor series of both $\tan^{-1}$ expressions in (3) coincide

$$
\begin{aligned}
\theta_i &= \left[\frac{1}{1 + h_{i+1}(0)^2} h'_{i+1}(0) - \frac{1}{1 + h_i(0)^2} h'_i(0) \right] \varepsilon + o(\varepsilon) \\
&\overset{(70)}{=} \frac{1}{1 + \left[\frac{\chi'(s_i) \cdot e_y}{\chi'(s_i) \cdot e_x}\right]^2} \frac{\chi''(s_i) \cdot \chi'_\perp(s_i)}{\left[\chi'(s_i) \cdot e_x\right]^2} \varepsilon + o(\varepsilon) \\
&= \frac{\chi''(s_i) \cdot \chi'_\perp(s_i)}{\|\chi'(s_i)\|^2} \varepsilon + o(\varepsilon) \overset{(11)}{=} \vartheta'(s_i)\varepsilon + o(\varepsilon) \,.
\end{aligned}
\tag{71}
$$

For the expansion (1), it is required to perform the expansion of the norm of a vector valued function $a(\varepsilon)$, i.e. $\|a(\varepsilon)\| = \|a(0)\| + \frac{a(0) \cdot a'(0)}{\|a(0)\|}\varepsilon + o(\varepsilon)$. Taking $a(\varepsilon)$ to be the expansions appearing in the squared brackets of (68) and considering that $\rho(s) = \|\chi'(s)\|$,

$$
\|p_{i\pm 1} - p_i\| = \varepsilon \left[\|\chi'(s_i)\| \pm \frac{\chi'(s_i) \cdot \chi''(s_i)}{\|\chi'(s_i)\|}\frac{\varepsilon}{2} + o(\varepsilon) \right] = \varepsilon \left[\rho(s_i) \pm \rho'(s_i)\frac{\varepsilon}{2} + o(\varepsilon) \right] \,.
\tag{72}
$$

Consequently, the expansion of the squared expression of (72) reads

$$
\|p_{i\pm 1} - p_i\|^2 = \varepsilon^2 \left[\|\chi'\|^2 \pm (\chi' \cdot \chi'')\varepsilon + o(\varepsilon) \right]_{s=s_i} = \varepsilon^2 \left[\rho^2 \pm \rho\rho'\varepsilon + o(\varepsilon) \right]_{s=s_i} \,.
\tag{73}
$$

Using (14), (72) and (73) in the argument of $\cos^{-1}$ of $(1)_{1,2}$,

$$
\begin{aligned}
h^{1D(S)}(\varepsilon) &= \left. \frac{\varepsilon^2 \left[\rho^2 - \rho\rho'\varepsilon + \varepsilon(1/\cos\gamma)(\tilde{l}^{1D(S)} - \tilde{l}^{2S(D)}) + o(\varepsilon) \right]}{2\varepsilon^2 \left[1/2\cos\gamma + \tilde{l}^{1D(S)}\varepsilon + o(\varepsilon) \right] \left[\rho - \rho'\frac{\varepsilon}{2} + o(\varepsilon) \right]} \right|_{s=s_i} \\
&= \left. \frac{\rho^2 + \varepsilon \left[(1/\cos\gamma)(\tilde{l}^{1D(S)} - \tilde{l}^{2S(D)}) - \rho\rho' \right] + o(\varepsilon)}{(1/\cos\gamma)\rho + \varepsilon \left[2\tilde{l}^{1D(S)}\rho - (1/2\cos\gamma)\rho' \right] + o(\varepsilon)} \right|_{s=s_i} \,.
\end{aligned}
\tag{74}
$$

Similarly, the expansions of the arguments of $\cos^{-1}$ appearing in $(1)_{3,4}$ read

$$
h^{2S(D)}(\varepsilon) = \left. \frac{\rho^2 + \varepsilon \left[(1/\cos\gamma)(\tilde{l}^{2S(D)} - \tilde{l}^{1D(S)}) - \rho\rho' \right] + o(\varepsilon)}{(1/\cos\gamma)\rho + \varepsilon \left[2\tilde{l}^{2S(D)}\rho - (1/2\cos\gamma)\rho' \right] + o(\varepsilon)} \right|_{s=s_i} \,.
\tag{75}
$$

All functions are of the form $h^{\mu\nu}(\varepsilon) = [a + \varepsilon b^{\mu\nu} + o(\varepsilon)] / [c + \varepsilon d^{\mu\nu} + o(\varepsilon)]$ with $h^{\mu\nu}(0) = a/c$ and $(h^{\mu\nu})'(0) = (b^{\mu\nu}c - d^{\mu\nu}a)/c^2$. The angles $\varphi_i^{\mu\nu}$ are thus expanded as

$$
\varphi_i^{\mu\nu} = \cos^{-1}[h^{\mu\nu}(0)] - \frac{\varepsilon}{\sqrt{1 - h^{\mu\nu}(0)^2}}(h^{\mu\nu})'(0) + o(\varepsilon) \,.
\tag{76}
$$

Expanding $\varphi_i^{\mu S} - \varphi_i^{\mu D}$ with the help of (76), the first term thereof cancels. Inserting the derivative with respect to ε evaluated at $\varepsilon = 0$ of (74) and (75)$_1$,

$$
\begin{aligned}
\varphi_i^{1S} - \varphi_i^{1D} &= \left.\frac{\rho^2(\tilde{l}^{1S} - \tilde{l}^{1D}) + (1/2\cos\gamma)\rho\rho' - (1/2\cos^2\gamma)(\tilde{l}^{1S} - \tilde{l}^{1D} + \tilde{l}^{2S} - \tilde{l}^{2D})}{\rho(1/2\cos\gamma)\sqrt{2}\sqrt{\frac{(1/\cos^2\gamma) - \rho^2}{2}}}\right|_{s=s_i} \varepsilon + o(\varepsilon) \\
&= \left.\frac{\rho[\rho^2 - (1/2\cos^2\gamma)](\tilde{l}^{1S} - \tilde{l}^{1D}) + (1/2\cos\gamma)\rho^2\rho' + \rho(1/2\cos^2\gamma)(\tilde{l}^{2D} - \tilde{l}^{2S})}{\rho^2(1/2\cos\gamma)\sqrt{2}\sqrt{\frac{(1/\cos^2\gamma) - \rho^2}{2}}}\right|_{s=s_i} \varepsilon + o(\varepsilon) \, .
\end{aligned}
\tag{77}
$$

In the same manner the expansion for the difference in angles of the oblique springs indexed by $\mu = 2$ is obtained. Moreover, the previous expressions are simplified to give

$$
\varphi_i^{1(2)S} - \varphi_i^{1(2)D} = \left.\frac{4[\rho^2 - (1/2\cos^2\gamma)](\tilde{l}^{1(2)S} - \tilde{l}^{1(2)D}) + (1/\cos\gamma)(\rho^2)' + (2/\cos^2\gamma)(\tilde{l}^{2(1)D} - \tilde{l}^{2(1)S})}{4\rho(1/2\cos\gamma)\sqrt{(1/\cos^2\gamma) - \rho^2}}\right|_{s=s_i} \varepsilon + o(\varepsilon)
\tag{78}
$$

which, for $\gamma = \pi/6$, becomes

$$
\varphi_i^{1(2)S} - \varphi_i^{1(2)D} = \left.\frac{\sqrt{3}(\rho^2 - 2/3)(\tilde{l}^{1(2)S} - \tilde{l}^{1(2)D}) + \rho\rho' + 2/\sqrt{3}(\tilde{l}^{2(1)D} - \tilde{l}^{2(1)S})}{\rho\sqrt{4/3 - \rho^2}}\right|_{s=s_i} \varepsilon + o(\varepsilon) \, .
\tag{79}
$$

Using (14), (72) and (73) in the argument of $\cos^{-1}$ of (2), we can compute

$$
\begin{aligned}
h^{1(2)}(\varepsilon) &= \frac{\left(l_i^{1(2)D}\right)^2 + \left(l_{i+1}^{2(1)S}\right)^2 - \|p_{i+1} - p_i\|^2}{2l_i^{1(2)D}l_{i+1}^{2(1)S}} \\
&= \left.\frac{\varepsilon^2\left[1/2\cos^2\gamma - \rho^2 + \rho\rho'\varepsilon + \varepsilon(1/\cos\gamma)(\tilde{l}^{1(2)D} + \tilde{l}^{2(1)S}) + o(\varepsilon)\right]}{2\varepsilon^2\left[1/2\cos\gamma + \tilde{l}^{1(2)D}\varepsilon + o(\varepsilon)\right]\left[1/2\cos\gamma + \tilde{l}^{2(1)S}\varepsilon + o(\varepsilon)\right]}\right|_{s=s_i} \\
&= \left.\frac{1/2\cos^2\gamma - \rho^2 + \varepsilon\left[\rho\rho' + (1/\cos\gamma)(\tilde{l}^{1(2)D} + \tilde{l}^{2(1)S})\right] + o(\varepsilon)}{1/2\cos^2\gamma + \varepsilon(1/\cos\gamma)(\tilde{l}^{1(2)D} + \tilde{l}^{2(1)S}) + o(\varepsilon)}\right|_{s=s_i} \, .
\end{aligned}
\tag{80}
$$

The angles ξ^1 and ξ^2 are thus expanded as

$$
\xi_i^\mu = \cos^{-1}\left[h^\mu(0)\right] + o(\varepsilon^0) = \left.\cos^{-1}\left(1 - \frac{\rho^2}{1/2\cos^2\gamma}\right)\right|_{s=s_i} + o(\varepsilon^0) \, .
\tag{81}
$$

Thus, for $\gamma = \pi/6$,

$$
\xi_i^\mu = \left.\cos^{-1}\left(1 - \frac{3}{2}\rho^2\right)\right|_{s=s_i} + o(\varepsilon^0) \, .
\tag{82}
$$

For the expansion of

$$
K_S\left[\cos^{-1}\left(1 - \frac{\rho_\alpha^2}{1/2\cos^2\gamma}\right) - \pi + 2\gamma\right]^2
\tag{83}
$$

in (47) with respect to ∇u required to get equation (52), equation (50) is inserted into the following

$$
a\left\{\cos^{-1}\left[1 - \frac{(x+1)^2}{1/2\cos^2 b}\right] + 2b - \pi\right\}^2 = [4a\cot b]x^2 + o(x^2)
\tag{84}
$$

with $a, b \in \mathbb{R}$ to get

$$
K_S\left[\cos^{-1}\left(1 - \frac{\rho_\alpha^2}{1/2\cos^2\gamma}\right) - \pi + 2\gamma\right]^2 = [4K_S\cot\gamma]\left(\frac{\partial u}{\partial\alpha}\cdot e_\alpha\right)^2 + o\left(\left\|\frac{\partial u}{\partial\alpha}\right\|^2\right) \, .
\tag{85}
$$

References

[1] Harrison P. 2016 Modelling the forming mechanics of engineering fabrics using a mutually constrained pantographic beam and membrane mesh. *Composites Part A: Applied Science and Manufacturing* **81**, 145–157.

[2] Andreaus U, dell'Isola F, Giorgio I, Placidi L, Lekszycki T, Rizzi N. 2016 Numerical simulations of classical problems in two-dimensional (non) linear second gradient elasticity. *International Journal of Engineering Science* **108**, 34–50.

[3] Auffray N, Dirrenberger J, Rosi G. 2015 A complete description of bi-dimensional anisotropic strain-gradient elasticity. *International Journal of Solids and Structures* **69**, 195–206.

[4] Battista A, Rosa L, dell'Erba R, Greco L. 2016 Numerical investigation of a particle system compared with first and second gradient continua: Deformation and fracture phenomena. *Mathematics and Mechanics of Solids* p. 1081286516657889.

[5] Steigmann DJ. 1996 The variational structure of a nonlinear theory for spatial lattices. *Meccanica* **31**, 441–455.

[6] Turco E, dell'Isola F, Rizzi N, Grygoruk R, Müller W, Liebold C. 2016a Fiber rupture in sheared planar pantographic sheets: Numerical and experimental evidence. *Mechanics Research Communications* **76**, 86–90.

[7] Turco E, Golaszewski M, Cazzani A, Rizzi N. 2016b Large deformations induced in planar pantographic sheets by loads applied on fibers: experimental validation of a discrete Lagrangian model. *Mechanics Research Communications* **76**, 51–56.

[8] Turco E, Barcz K, Pawlikowski M, Rizzi N. 2016c Non-standard coupled extensional and bending bias tests for planar pantographic lattices. Part I: numerical simulations. *Zeitschrift für angewandte Mathematik und Physik* **67**, 122.

[9] Turco E, Giorgio I, Misra A, dell'Isola F. 2017 King post truss as a motif for internal structure of (meta) material with controlled elastic properties. *Royal Society Open Science* **4**.

[10] Turco E, dell'Isola F, Cazzani A, Rizzi N. 2016 Hencky-type discrete model for pantographic structures: numerical comparison with second gradient continuum models. *Zeitschrift für angewandte Mathematik und Physik* **67**.

[11] dell'Isola F, Giorgio I, Pawlikowski M, Rizzi NL. 2016 Large deformations of planar extensible beams and pantographic lattices: heuristic homogenization, experimental and numerical examples of equilibrium. *Proc. R. Soc. A* **472**.

[12] Babuška I. 1976 Homogenization approach in engineering. In *Computing methods in applied sciences and engineering* pp. 137–153. Springer.

[13] Allaire G. 1992 Homogenization and two-scale convergence. *SIAM Journal on Mathematical Analysis* **23**, 1482–1518.

[14] Tartar L. 2009 *The general theory of homogenization: a personalized introduction* vol. 7. Springer Science & Business Media.

[15] Yu W, Tang T. 2009 Variational asymptotic method for unit cell homogenization. In *Advances in Mathematical Modeling and Experimental Methods for Materials and Structures* pp. 117–130. Springer.

[16] dell'Isola F, Maier G, Perego U, Andreaus U, Esposito R, Forest S. 2014 The complete works of Gabrio Piola: volume I. *Cham, Switzerland: Springer.*

[17] Golaszewski M, Grygoruk R, Giorgio I, Laudato M, Di Cosmo F. 2018 Metamaterials with relative displacements in their microstructure: technological challenges in 3D printing, experiments and numerical predictions. *Continuum Mechanics and Thermodynamics* pp. 1–20.

[18] Milton G, Briane M, Harutyunyan D. 2017a On the possible effective elasticity tensors of 2-dimensional and 3-dimensional printed materials. *Math. and Mech. of Comp. Sys.* **5**, 41–94.

[19] Milton G, Harutyunyan D, Briane M. 2017b Towards a complete characterization of the effective elasticity tensors of mixtures of an elastic phase and an almost rigid phase. *Mathematics and Mechanics of Complex Systems* **5**, 95–113.

[20] Abdoul-Anziz H, Seppecher P. 2018 Strain gradient and generalized continua obtained by homogenizing frame lattices. *Mathematics and Mechanics of Complex Systems.*

[21] Barchiesi E, Spagnuolo M, Placidi L. 2018 Mechanical metamaterials: a state of the art. *Mathematics and Mechanics of Solids.*

[22] Di Cosmo F, Laudato M, Spagnuolo M. 2018 Acoustic Metamaterials Based on Local Resonances: Homogenization, Optimization and Applications. In *Generalized Models and Non-classical Approaches in Complex Materials 1* pp. 247–274. Springer.

[23] dell'Isola F, Lekszycki T, Pawlikowski M, Grygoruk R, Greco L. 2015 Designing a light fabric metamaterial being highly macroscopically tough under directional extension: first experimental evidence. *Zeitschrift für angewandte Mathematik und Physik* **66**, 3473–3498.

[24] Giorgio I, Della Corte A, dell'Isola F, Steigmann DJ. 2016 Buckling modes in pantographic lattices. *Comptes rendus Mecanique* **344**, 487–501.

[25] Giorgio I, Della Corte A, dell'Isola F. 2017 Dynamics of 1D nonlinear pantographic continua. *Nonlinear Dynamics* **88**, 21–31.

[26] Placidi L, Barchiesi E, Turco E, Rizzi N. 2016a A review on 2D models for the description of pantographic fabrics. *Zeitschrift für angewandte Mathematik und Physik* **67(5)**.

[27] Placidi L, Andreaus U, Giorgio I. 2016b Identification of two-dimensional pantographic structure via a linear D4 orthotropic second gradient elastic model. *Journal of Engineering Mathematics* pp. 1–21.

[28] Giorgio I. 2016 Numerical identification procedure between a micro-Cauchy model and a macro-second gradient model for planar pantographic structures. *Zeitschrift für angewandte Mathematik und Physik* **67**(4).

[29] Cuomo M, dell'Isola F, Greco L. 2016 Simplified analysis of a generalized bias test for fabrics with two families of inextensible fibres. *Zeitschrift für angewandte Mathematik und Physik* **67**.

[30] Turco E, Misra A, Pawlikowski M, dell'Isola F, Hild F. 2018 Enhanced Piola–Hencky discrete models for pantographic sheets with pivots without deformation energy: Numerics and experiments. *International Journal of Solids and Structures*.

[31] Misra A, Lekszycki T, Giorgio I, Ganzosch G, Müller WH, dell'Isola F. 2018 Pantographic metamaterials show atypical Poynting effect reversal. *Mech. Res. Commun.* **89**, 6–10.

[32] Eremeyev VA, dell'Isola F, Boutin C, Steigmann D. 2017 Linear pantographic sheets: existence and uniqueness of weak solutions. *Journal of Elasticity* pp. 1–22.

[33] Barchiesi E, dell'Isola F, Laudato M, Placidi L, Seppecher P. 2018 A 1D Continuum Model for Beams with Pantographic Microstructure: Asymptotic Micro-Macro Identification and Numerical Results. In *Advances in Mech. of Microstruct. Media and Struct.* pp. 43–74. Springer.

[34] Alibert JJ, Seppecher P, dell'Isola F. 2003 Truss modular beams with deformation energy depending on higher displacement gradients. *Mathematics and Mechanics of Solids* **8**, 51–73.

[35] Seppecher P, Alibert JJ, dell'Isola F. 2011 Linear elastic trusses leading to continua with exotic mechanical interactions. In *Journal of Physics: Conference Series* vol. 319 p. 012018. IOP Publishing.

[36] Barchiesi E, Eugster SR, Placidi L, dell'Isola F. 2019 Pantographic beam: a complete second gradient 1D-continuum in plane. *Zeitschrift für angewandte Mathematik und Physik* **70**, 135.

[37] dell Isola F, Seppecher P, Della Corte A. 2015 The postulations á la D'Alembert and á la Cauchy for higher gradient continuum theories are equivalent: a review of existing results. In *Proc. R. Soc. A* vol. 471. The Royal Society.

[38] dell'Isola F, Madeo A, Seppecher P. 2016 Cauchy tetrahedron argument applied to higher contact interactions. *Archive for Rational Mechanics and Analysis* **219**, 1305–1341.

[39] dell'Isola F, Steigmann D. 2015 A two-dimensional gradient-elasticity theory for woven fabrics. *J. Elasticity* **18**, 113–125.

[40] Eugster SR, Glocker C. 2017 On the notion of stress in classical continuum mechanics. *Mathematics and Mechanics of Complex Systems* **5**, 299–338.

[41] Steigmann D, Faulkner M. 1993 Variational theory for spatial rods. *Journal of Elasticity* **33**, 1–26.

[42] Germain P. 1973 The Method of Virtual Power in Continuum Mechanics. Part 2: Microstructure. *SIAM Journal on Applied Mathematics* **25**, 556–575.

[43] Forest S, Sievert R. 2006 Nonlinear microstrain theories. *International Journal of Solids and Structures* **43**, 7224 – 7245. Size-dependent Mechanics of Materials.

[44] Eremeyev VA, Lebedev LP, Altenbach H. 2012 *Foundations of micropolar mechanics*. Springer Science & Business Media.

[45] Altenbach H, Bîrsan M, Eremeyev VA. 2013 Cosserat-type rods. In *Generalized Continua from the Theory to Engineering Applications* pp. 179–248. Springer.

[46] Auffray N, dell'Isola F, Eremeyev V, Madeo A, Rosi G. 2015 Analytical continuum mechanics à la Hamilton–Piola least action principle for second gradient continua and capillary fluids. *Mathematics and Mechanics of Solids* **20**, 375–417.

[47] Bersani A, dell'Isola F, Seppecher P Lagrange multipliers in infinite dimensional spaces, examples of application. In Altenbach H, Öchsner A, editors, *Encyclopedia of Continuum Mechanics*.

[48] Abali B, Müller W, Eremeyev V. 2015 Strain gradient elasticity with geometric nonlinearities and its computational evaluation. *Mechanics of Advanced Materials and Modern Processes* **1**, 4.

[49] Abali BE, Müller WH, dell'Isola F. 2017 Theory and computation of higher gradient elasticity theories based on action principles. *Archive of Applied Mechanics* **87**, 1495–1510.

[50] Spagnuolo M, Barcz K, Pfaff A, dell'Isola F, Franciosi P. 2017 Qualitative pivot damage analysis in aluminum printed pantographic sheets: numerics and experiments. *Mechanics Research Communications* **83**, 47–52.

[51] Spagnuolo M, Peyre P, Dupuy C. 2019 Phenomenological aspects of quasi-perfect pivots in metallic pantographic structures. *Mechanics Research Communications* p. 103415.

[52] De Angelo M, Spagnuolo M, D'Annibale F, Pfaff A, Hoschke K, Misra A, Dupuy C, Peyre P, Dirrenberger J, Pawlikowski M. 2019 The macroscopic behavior of pantographic sheets depends mainly on their microstructure: experimental evidence and qualitative analysis of damage in metallic specimens. *Continuum Mechanics and Thermodynamics* pp. 1–23.

[53] Misra A, Singh V. 2013 Micromechanical model for viscoelastic materials undergoing damage. *Continuum Mechanics and Thermodynamics* pp. 1–16.

[54] Misra A, Poorsolhjouy P. 2015 Granular micromechanics model for damage and plasticity of cementitious materials based upon thermomechanics. *Mathematics and Mechanics of Solids* p. 1081286515576821.

[55] Misra A, Singh V. 2015 Thermomechanics-based nonlinear rate-dependent coupled damage-plasticity granular micromechanics model. *Continuum Mechanics and Thermodynamics* **27**, 787.

[56] Misra A, Ching W. 2013 Theoretical nonlinear response of complex single crystal under multi-axial tensile loading. *Scientific Reports* **3**, 1488.

[57] Sutton M, McNeill S, Helm J, Chao Y. 2000 pp. 323–372. In *Advances in Two-Dimensional and Three-Dimensional Computer Vision*, vol. Topics in Appl. Phys., 77, pp. 323–372. Berlin (Germany): Springer.

[58] Sutton M, Orteu J, Schreier H. 2009 *Image correlation for shape, motion and deformation measurements: Basic Concepts, Theory and Applications*. New York, NY (USA): Springer.

[59] Sutton M. 2013 Computer Vision-Based, Noncontacting Deformation Measurements in Mechanics: A Generational Transformation. *Appl. Mech. Rev.* **65**, 050802.

[60] Peters W, Ranson W. 1982 Digital imaging techniques in experimental stress analysis. *Opt. Eng.* **21**, 427–431.

[61] Sutton M, Wolters W, Peters W, Ranson W, McNeill S. 1983 Determination of Displacements Using an Improved Digital Correlation Method. *Im. Vis. Comp.* **1**, 133–139.

[62] Chu T, Ranson W, Sutton M, Peters W. 1985 Applications of Digital-Image-Correlation Techniques to Experimental Mechanics. *Exp. Mech.* **3**, 232–244.

[63] Broggiato G. 2004 Adaptive image correlation technique for full-field strain measurement. In Pappalettere C, editor, *12th Int. Conf. Exp. Mech.* pp. 420–421. McGraw Hill, Lilan (Italy).

[64] Sun Y, Pang J, Wong C, Su F. 2005 Finite-element formulation for a digital image correlation method. *Appl. Optics* **44**, 7357–7363.

[65] Besnard G, Hild F, Roux S. 2006 "Finite-element" displacement fields analysis from digital images: Application to Portevin-Le Chatelier bands. *Exp. Mech.* **46**, 789–803.

[66] Turco E, Misra A, Pawlikowski M, dell'Isola F, Hild F. 2018 Enhanced Piola-Hencky discrete models for pantographic sheets with pivots without deformation energy: Numerics and experiments. *International Journal of Solids and Structures* **147**, 94–109.

[67] dell'Isola F, Seppecher P, Alibert JJ, Lekszycki T, Grygoruk R, Pawlikowski M, Steigmann D, Giorgio I, Andreaus U, Turco E, Golaszewski M, Rizzi N, Boutin C, Eremeyev V, Misra A, Placidi L, Barchiesi E, Greco L, Cuomo M, Cazzani A, Corte A, Battista A, Scerrato D, Zurba Eremeeva I, Rahali Y, Ganghoffer JF, Müller W, Ganzosch G, Spagnuolo M, Pfaff A, Barcz K, Hoschke K, Neggers J, Hild F. 2019 Pantographic metamaterials: an example of mathematically- driven design and of its technological challenges. *Cont. Mech. Thermod.*

[68] Hild F, Raka B, Baudequin M, Roux S, Cantelaube F. 2002 Multi-Scale Displacement Field Measurements of Compressed Mineral Wool Samples by Digital Image Correlation. *Appl. Optics* **IP 41**, 6815–6828.

[69] Barker D, Fourney M. 1977 Measuring fluid velocities with speckle patterns. *Optics Lett.* **1**, 135–137.

[70] Dudderar T, Simpkins P. 1977 Laser Speckle Photography in a Fluid Medium. *Nature* **270**, 45–47.

[71] Grousson R, Mallick S. 1977 Study of flow pattern in a fluid by scattered laser light. *Appl. Optics* **16**, 2334–2336.

[72] Adrian R. 1984 Scattering particle characteristics and their effect on pulsed laser measurements of fluid flow: speckle velocimetry vs. particle image velocimetry. *Appl. Optics* **23**, 1690–1691.

[73] Adrian R. 2005 Twenty years of particle image velocimetry. *Exp. Fluids* **39**, 159–169.

[74] Hild F, Roux S. 2012 Digital Image Correlation. In Rastogi P, Hack E, editors, *Optical Methods for Solid Mechanics. A Full-Field Approach* pp. 183–228 Weinheim (Germany). Wiley-VCH.

[75] Barchiesi E, Laudato M, Di Cosmo F. 2018 Wave dispersion in non-linear pantographic beams. *Mechanics Research Communications* **94**, 128–132.

[76] Giorgio I, Rizzi N, Turco E. 2017 Continuum modelling of pantographic sheets for out-of-plane bifurcation and vibrational analysis. *Proceedings of the Royal Society A: Mathematical, Physical and Engineering Sciences* **473**, 20170636.

Emilio Barchiesi
Dipartimento di Ingegneria Strutturale e Geotecnica, Università degli Studi di Roma "La Sapienza", Italy
International Research Center M&MoCS, Università degli Studi dell'Aquila, Italy
e-mail: BarchiesiEmilio@gmail.com

Simon R. Eugster
Institute for Nonlinear Mechanics, University of Stuttgart, Germany

Francesco dell'Isola
Dipartimento di Ingegneria Civile, Edile-Architettura e Ambientale, Università degli Studi dell'Aquila, Italy
Dipartimento di Ingegneria Strutturale e Geotecnica, Università degli Studi di Roma "La Sapienza", Italy
International Research Center M&MoCS, Università degli Studi dell'Aquila, Italy

François Hild
Laboratoire de Mécanique et Technologie (LMT) ENS Paris-Saclay/CNRS/Univ. Paris-Saclay, France